Polytechnic University of Marche

PhD Program in Biomedical Sciences
XXXVI Cycle
Department of Odontostomatologic and Specialized Clinical Sciences

Synchrotron-based Phase-Contrast High Resolution Tomography of Collagen Organization in Physiologic, Pathologic and Engineered Tissues

Supervisor:

Prof. Alessandra Giuliani

Ph.D Candidate:

Michele Furlani

Table of Contents

Acknowledgements

This work comes from three years of exploration. Exploration of what doing research means and exploration of fascinating and innovative ways of approaching a truth, which we are sure lies hidden in the architecture of an ubiquitous, though often neglected, tissue of our bodies.

Leading this exploration my supervisor, Professor Alessandra Giuliani, who has never been reluctant to show her passion for research and, I don't know how willingly, has also allowed mine to ignite. I learnt from her what it means to deal with disappointing results, as well as blatant ones, and to gain new knowledge in both cases. And I think this encapsulates the essence of research.

I would like to express my gratitude to Professor Giuliana Tromba and her SYRMEP team at the Elettra Synchrotron beamline. The opportunity to access the facility several times in this period was precious, and I did my best to observe and learn every aspect I had the chance to face during the experiments.

Special thanks to all the research groups I had the fortune to collaborate with, within and outside our University. Thanks for all the time and the endurance spent to understand each other. It has been time of immense value.

I would like to thank all the CISMiN group, who received me and allowed me to assimilate various characterization techniques.

I am also grateful to Maria Laura, because taking the first steps is way easier with someone else at your side, and to Nicole for the daily support, sharing and “screen paintings”.

Lastly, I would also like to extend my gratitude to Elettra: she always encourages and motivates me by showing me the best part of myself, depicted in her loving eyes.

Abstract

In this dissertation the results obtained during my PhD Course in the field of soft tissue imaging, in particular collagen tissue, using Synchrotron Radiation Phase Contrast High Resolution Tomography (PhC-μCT) will be presented.

In the Introduction, useful elements will be provided to allow the reader to understand the state of the art of morphological and morphometric studies on collagen-based tissues, including an excursus of the implications known to date in physiological and pathological processes and in relation to what is still debated on its functions.

This will be followed by a description of the imaging techniques most used in scientific research to investigate the structure of collagen-based tissues and, more recently, their involvement in numerous processes. Particular relevance will then be given to PhC-μCT, detailing the existing setups available at Synchrotron facilities and describing the procedure to obtain the final image.

The central portion of this dissertation will describe some of the results obtained during the Doctoral Course in different physio-pathological contexts: in the physiological repair of tissues after abutment implantation; in the pathological triggering of fibrotic processes in an animal model of scleroderma, as well as, on human samples, the correlations between collagen tissues and tumor, in two circumstances: uterine leiomyomas and oral squamous cell carcinoma.

At the conclusion of this dissertation, some interesting future developments will be evaluated and discussed for the continuation of research in these areas of study.

1 Introduction

This chapter is designed to allow the reader to approach the results presented in this dissertation with the required awareness of which the structural features of the collagenous tissue are, which steps have already been taken in the research of its functions, and which question are still pending unanswered.

1.1 Collagen composition, properties and mechanical behavior

Collagen is an essential fibrous protein in the human body. It serves as a cornerstone for structural integrity and biomechanical function across various tissues. With 28 distinct proteins within its family, collagen assumes a ubiquitous presence in connective tissues like skin, bones, tendons, ligaments, and blood vessels. Its diverse forms contribute to the robustness, resilience, and flexibility of these vital structures.

Collagen Type I is the most abundant collagen in the human body, constituting about 90% of the body's total collagen content. It is primarily found in bones, tendons and skin providing strength and structural support. The other types of collagen, such as Type II, III, IV, V, and others, are present in smaller quantities and serve different functions in various tissues. Collagen Type II is primarily found in cartilage, providing resilience and support. Collagen Type III is often found alongside Type I in skin, blood vessels, and internal organs, contributing to the elasticity and flexibility of these tissues. Collagen Type IV is a major component of basement membranes, providing structural support and facilitating filtration in tissues. Collagen Type V is found in various tissues, including skin, tendons, and placenta, playing a role in regulating the assembly of other collagen types.

Collagen's presence in interstitial tissue provides both mechanical strength and porosity, facilitating nutrient transport and cell migration. These networks exhibit adaptability, for instance aligning in thick fibers in weight-bearing tendons for optimized force

transmission, while in the cornea, they interweave into thin sheets to maintain strength alongside optical transparency. [1]

As its various types may suggest, beyond its structural role, collagen profoundly influences cellular behavior within tissues. Collagen fibers serve as conduits for topographical, biochemical, and mechanical signals that regulate cellular processes like proliferation, differentiation, migration, and apoptosis. This mechanobiological interplay between cells and the surrounding collagen matrix is pivotal in guiding physiological processes such as wound healing but can also provoke pathological responses. [2] Aberrant stiffening of interstitial collagen networks, for instance, can promote invasive cell behavior associated with fibrosis, cancer, and metastasis. [3]–[7]

Initially, only from a treatment-oriented perspective, literature provided insight on how forces impact collagen integrity and functionality. In physiology, this principle is known as Davis's Law, positing that soft tissue conforms its structure according to the patterns of stress exerted upon it [8]. Named after Dr. Henry Gassett Davis, an American orthopedic surgeon who described the principle in the late 19th century, Davis's Law suggests that when soft tissues are subjected to increased tension or stress over time, they will adapt by becoming stronger and more resistant to that particular type of stress. Conversely, when they are subjected to disuse or reduced stress, they will weaken and atrophy. Mechanical forces can induce structural changes in connective tissue and play a crucial role in the formation and maintenance of collagen, while immobilization and stress deprivation can negatively affect connective tissue integrity. [9]

In understanding the mechanical properties of connective tissues, a pivotal focus lies on the collagenous components, from the amino-acid sequence to fibrils and fibers. Among the 28 types, II, III, V, XI, XXVII, along with type I, the most common and abundant, are fibril-forming protein. Similarly to other proteins, four different structural levels can be identified for these collagen types, with one level (i.e., primary) at the atomic/submolecular scale, two levels at the molecular scale (i.e., secondary and tertiary), and one level at the supramolecular scale (i.e., quaternary) [10] (**Figure 1**).

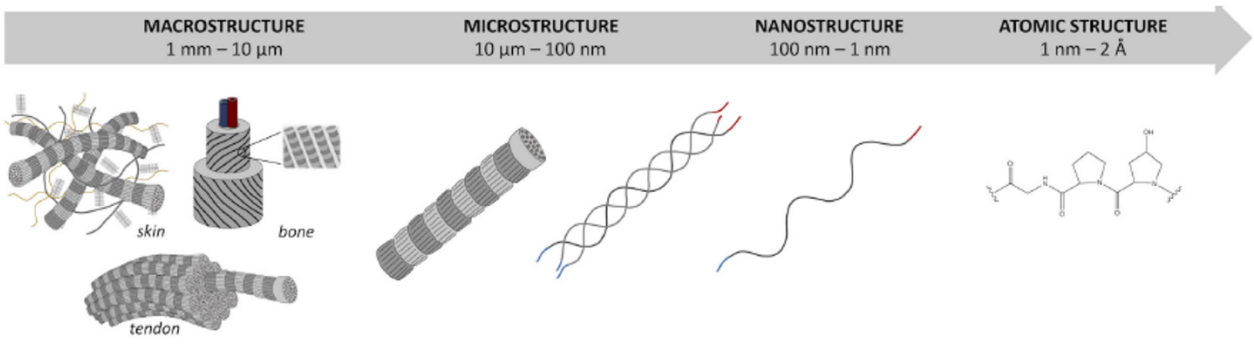

Structural level	Length scale	Collagen's feature	Biological activity
Primary	2 Å–1 nm	Amino acid sequence	• Cell ligand identity
Secondary and tertiary	≈10–100 nm	Molecular conformation • PPII helices–secondary • Triple helix–tertiary	• Cell ligand identity • Cell ligand exposure • Enzymatic resistance and degradation mechanism • Mechanical strength/mechanotransduction* • Antigenicity (for animal-derived collagen used as a biomaterial)
Quaternary	≈1 µm	Packing of molecules • Fibril structure – banding	• Enzymatic resistance • Mechanical strength/mechanotransduction* • Activation of blood clotting
Architecture	≈1–10 mm	Packing of fibrils • Fiber structure • Fiber arrangement or orientation	• Tissue mechanical properties (e.g., stiffness)/mechanotransduction* • Tissue functionality

*By means of mechanotransduction, cells can detect mechanical stimuli from their microenvironment and respond by performing biological processes.

Figure 1 – *The hierarchical structure of collagen's most common proteins, the fibril-forming ones, their dimensional scale and how they interact with their biological surrounding. (edited from [10], CC-BY 4.0)*

Collagen consists of tropocollagen (TC) molecules that have lengths of about 100 nm with approximately 1.5 nm in diameter. Staggered arrays of TC molecules form fibrils, which arrange to form collagen fibers. The actual structural hierarchy of collagen starts from the triple-helical collagen molecules, first proposed in 1951 by Pauling [11]; the triple helix motif defines the protein as collagen, is its fingerprint in all the 28 variants of this protein. These structural elements play a fundamental role in conferring appropriate mechanical characteristics to tissues across a diverse array of functions. From providing tensile strength to resisting plastic deformation and crack propagation, collagen's contributions are significant. However, unraveling the intricate interplay between collagen's structural features and tissue mechanics remains a complex endeavor. Parry [12], [13] delved into the nuanced structural and functional aspects of collagen within connective tissues, aiming to shed light on how these elements bestow mechanical resilience and integrity upon tissues with varying functions.

- Collagen Fibrils and Cross-Links: Despite low flexion or torsion strength, collagen fibrils exhibit high tensile strength due to intermolecular covalent cross-links. These cross-links become stable as tissues mature, linking collagen molecules both axially and laterally.
- Fibril Diameter Distribution: The distribution of collagen fibril diameters significantly influences tissue mechanical properties. Small-diameter fibrils contribute to creep inhibition, while large-diameter fibrils enhance the tissue's ability to withstand high stress levels.
- Critical Fibril Length: Collagen fibrils must exceed a critical length to act as high-tensile elements without being pulled out of the tissue. This length increases with fibril diameter, emphasizing the importance of shear stress at the fibril/matrix interface.
- Collagen Content: Tissues with higher collagen content per unit mass exhibit greater tensile strength. While larger diameter fibrils correlate with higher collagen content, an appropriate distribution of fibril diameters can also enhance creep resistance.
- Fibril-Matrix Structure: The fibril-matrix nature of connective tissues enhances their ability to withstand crack propagation, preventing permanent tissue damage even if individual fibrils are damaged.
- Fibril Orientation: Collagen fibril orientation varies across tissues and influences their mechanical properties. Fibrils oriented parallel to the direction of stress provide optimal tensile strength, while misaligned fibrils may decrease strength/weight ratios.
- Collagen Fibers: Collagen fibers, composed of interwoven fibrils, exhibit features such as mobility between fibers and a macroscopic crimp structure. These properties contribute to linking fibers together and preventing permanent tissue damage under stress.

Tissues consist of networks of fibril bundles, organized hierarchically across different length scales, contributing to the overall mechanical response at the tissue level. Such considerations on collagen's structure and mechanics have been foundational in understanding tissue function and dysfunction. Collagen exhibits non-linear elasticity,

stiffening in response to deformation, a crucial trait for providing mechanical stability under varying strain levels (**Figure 2**). However, the intricate architecture of collagenous tissues presents challenges in identifying the structural basis of this stiffening response. [14]

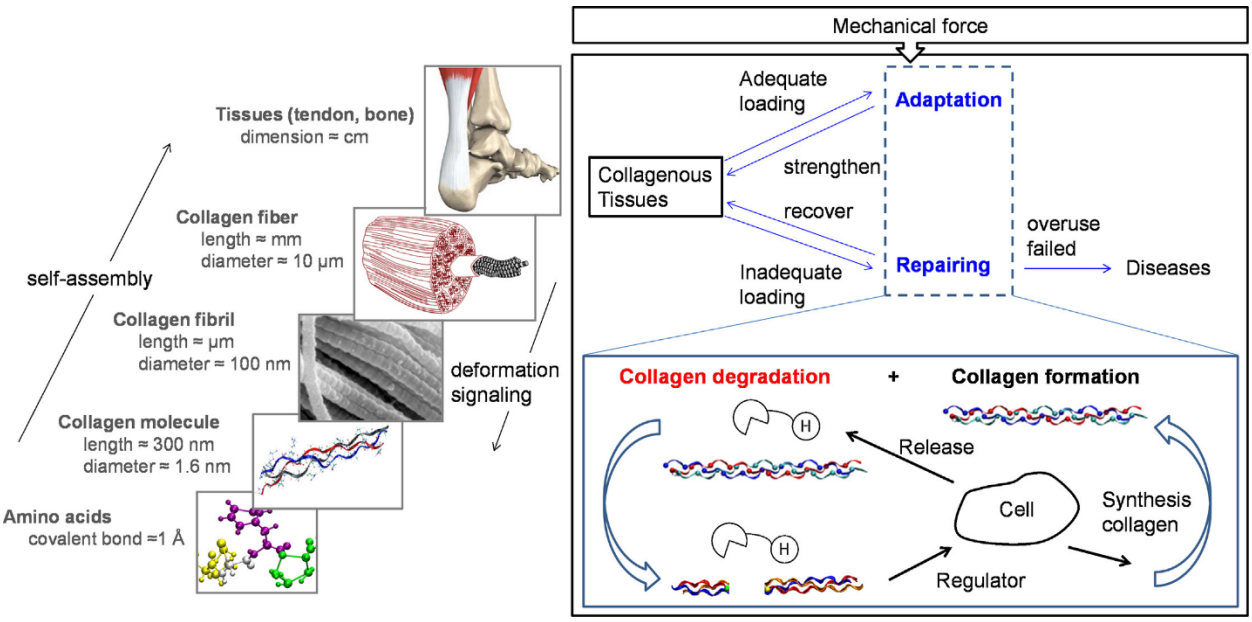

Figure 2 - *Structure of collagenous tissues and a schematic of biomechanics of collagen materials. Collagenous tissues are hierarchical structures composed of self-assembled collagen molecules. They are materials which can sense the mechanical forces, turning in to signals through deformation at molecule level, to enable tissue remodeling and repairing. Adequate loading enables the adaptation to strengthen the collagenous tissue while inadequate loading may lead to injuries. ([7], CC-BY 4.0 - left panel from A. Gautieri, et al. Nano Lett. (2011). Hierarchical structure of connective tissues Copyright 2011 American Chemical society)*

Recent advancements have illuminated the nanomechanics of collagen microfibrils, revealing the indispensable role of hierarchical composition in imparting key mechanical properties such as extensibility, strain hardening and toughness. Notably, collagen molecules alone are insufficient to meet the wide range of mechanical functionality required for tissue physiology. Instead, a multitude of deformation mechanisms, stemming from the material's hierarchical composition, are critical for imparting essential mechanical properties.

Gautieri et al. [15] developed a full atomistic model of the mechanics of collagen microfibrils, which overcomes the limitations of previous models that did not account for biochemical details and were smaller in size compared to the typical length-scales of collagen molecules found in collagen microfibrils and fibrils. Previous models also did not consider the additional interfaces and disorder that may exist between larger-scale collagen fibrils, which could affect the mechanical properties. The computational method used in the study involved all-atom simulations of the collagen microfibril and found that the mechanical properties of collagen microfibrils differ significantly from single collagen molecules. Moreover, they obtained from their model that Young's modulus of collagen microfibrils is a few hundred megapascals, which is consistent with experimental data.

Collagen's multifaceted roles in tissue physiology, pathology, and biomechanics underscore its significance in human health and disease. The integration of collagen into the study of biomechanics has yielded valuable insights into tissue function and dysfunction, with implications for therapeutic interventions and clinical management.

1.2 How to investigate collagen – Imaging Methods

The techniques commonly adopted in scientific research to observe and study the morphological characteristics of collagen will be briefly described below. Each of them presents strengths which consent unique capabilities and approach of analysis. Different levels of analysis may lead researchers to lean towards one or the other technique as their needs change from a higher to a lower magnification scale, different temporal resolution, to real-time imaging, and of course, planar imaging versus three-dimensional tissue assessment.

1.2.1 Histology

Histology techniques have been developed over the centuries to study the cellular organization of body tissues and organs. These techniques involve various steps such as tissue fixation, embedding, sectioning, staining, and finally imaging. Different staining methods are used to study tissue characteristics and microscopic structures, including immunohistochemistry, in situ hybridization, Sudan staining, Sirius Red staining, Masson's trichrome staining and routine Hematoxylin and Eosin (H&E) staining [16]. In recent years, new histological techniques have been devised to overcome the limitations of traditional methods. These include cytoplasm-specific/nucleus-specific X-ray staining for 3-D histology, tissue clearing techniques, and advanced in situ sequencing techniques [17]. Histology relies on the preparation and microscopic examination of thin tissue sections.

Main applications:

- Visualizing cellular and tissue architecture.
- Identifying different tissue types and structures based on staining patterns.
- Examining pathological changes and disease states.

Histological techniques, such as hematoxylin and eosin (H&E) staining or Masson's trichrome staining, highlight collagen fibers based on their affinity for specific dyes. This allows for the visualization of collagen organization, distribution, and density, and alterations in various pathological conditions.

Histology studies on collagen tissue have been conducted recently. One study proposed a polychromatic polarization microscope (PPM) that allows visualization of collagen fibers with color representation of fiber orientation and alignment using a regular microscope [18]. Another study showed that collagen content can be quantified from routine Hematoxylin and Eosin (HE) stained images alone, without the need for additional staining with Saffron (**Figure 3**) [19]. Moreover, a universal convolutional neural network (UCNN) was developed to classify histology images of burn-induced scar tissues and characterize collagen fiber organization, achieving high classification accuracies [20]. Additionally, an alternative label-free imaging approach called LC-PolScope was explored, which demonstrated good correlation with Second Harmonic Generation (SHG) microscopy in measuring collagen organization in thin histology sections [21].

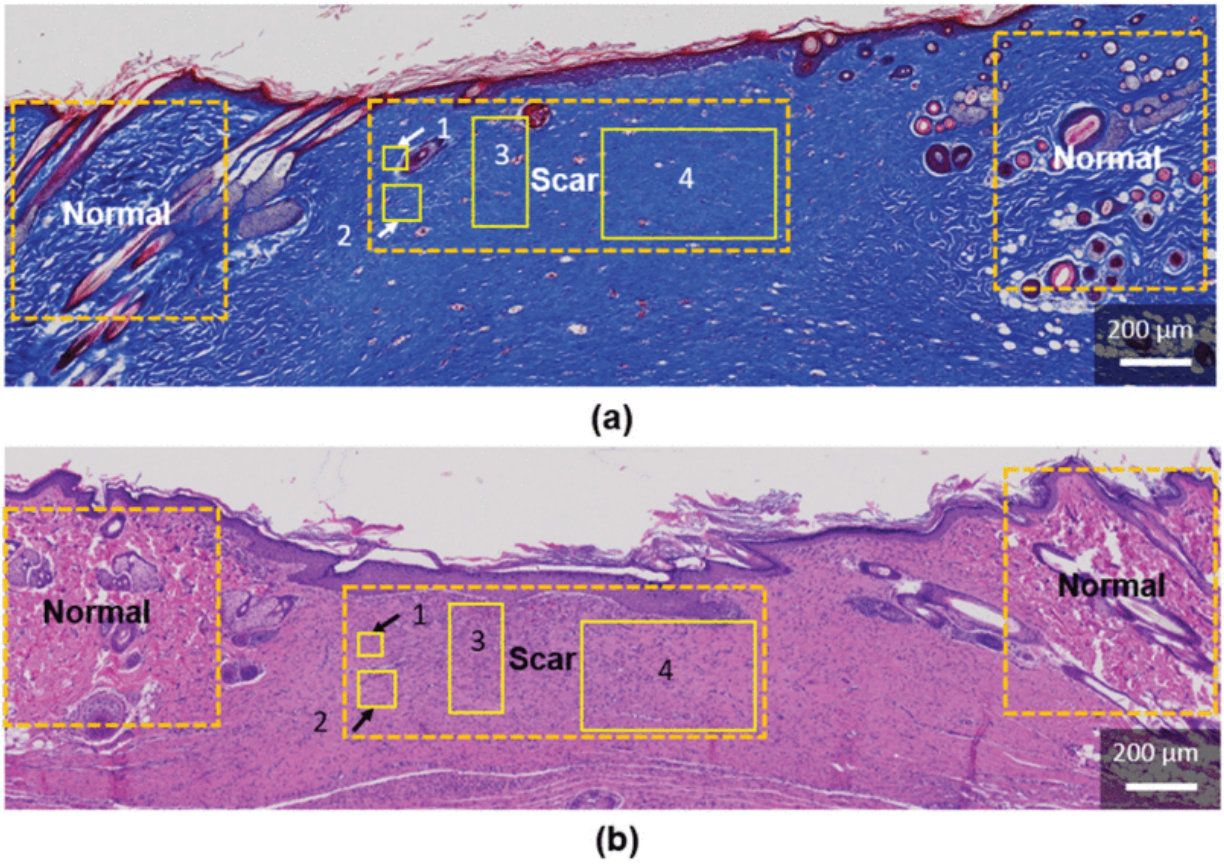

Figure 3 - *Photomicrograph of wounded skin tissue stained with (a) MT, (b) H&E. The orange-dashed boxes on the left and right sides show the normal tissue regions (as the control) that consist of coarse collagen fibers with skin appendages. The orange dashed box in the middle of the image represents the burn-induced scar tissue region with fine collagen fibers. The three solid yellow boxes inside the scar region are examples of ROIs of various sizes (*[19], *CC-BY 4.0).*

1.2.2 Second Harmonic Generation

The physical principle behind Second Harmonic Generation (SHG) imaging is a nonlinear optical process called second-harmonic generation. In SHG, two photons of the same frequency interact with a nonlinear medium, resulting in the generation of a new photon with twice the frequency (half the wavelength) of the incident photons. This phenomenon was first reported in the 1960s and is commonly used to characterize the second-order non-linear optical response of materials, especially in biomedical research. It occurs without the need for external labels or dyes, but only in materials with a non-centrosymmetric crystalline structure or in non-centrosymmetric environments, such as collagen fibers in biological tissues. In these materials, the electric dipole moments

produced by the nonlinear response of the molecules lead to the constructive interference of the incident photons, resulting in SHG emission.

In SHG imaging, a laser light source is typically used to generate the incident photons. By scanning the sample with the laser beam and detecting the SHG signal, high-resolution images of collagen fibers or other non-centrosymmetric structures within biological tissues can be obtained. The SHG signal provides label-free contrast and high spatial resolution, making it valuable for imaging tissue morphology and organization in various biomedical applications [22].

Main Applications:

- Imaging collagen in tissues such as skin, tendons, cartilage
- Dermatology, to investigate conditions like aging, scarring, and various skin disorders
- Neuroscience, neuronal connectivity, tissue architecture, and neurodegenerative diseases.

SHG is advantageous for capturing images of collagen fibers specifically due to its property of generating second harmonics in the spectral region between 400 and 500 nm, allowing to capture images of collagen fibers only, without interference from other signals. This specificity enables the extraction of structural and functional information from collagen fibers in tissues [23]. The high resolution achievable is essential for studying collagen fiber orientation, waviness, density, and dimensions accurately, contributing to a better understanding of tissue microstructure and function [24]. In dermatology it has been employed to explore its potential to differentiate collagen changes associated with different Basal Cell Carcinoma (BCC) subtypes, compared to normal skin structures and benign lesions (**Figure 4**) [25].

SHG has been employed to study conformational changes in biomolecules upon ligand binding, offering insights into a wide range of targets from soluble proteins to oligonucleotides. These applications showcase SHG microscopy as a versatile and powerful tool for understanding biological structures and processes in biomedical research [26].

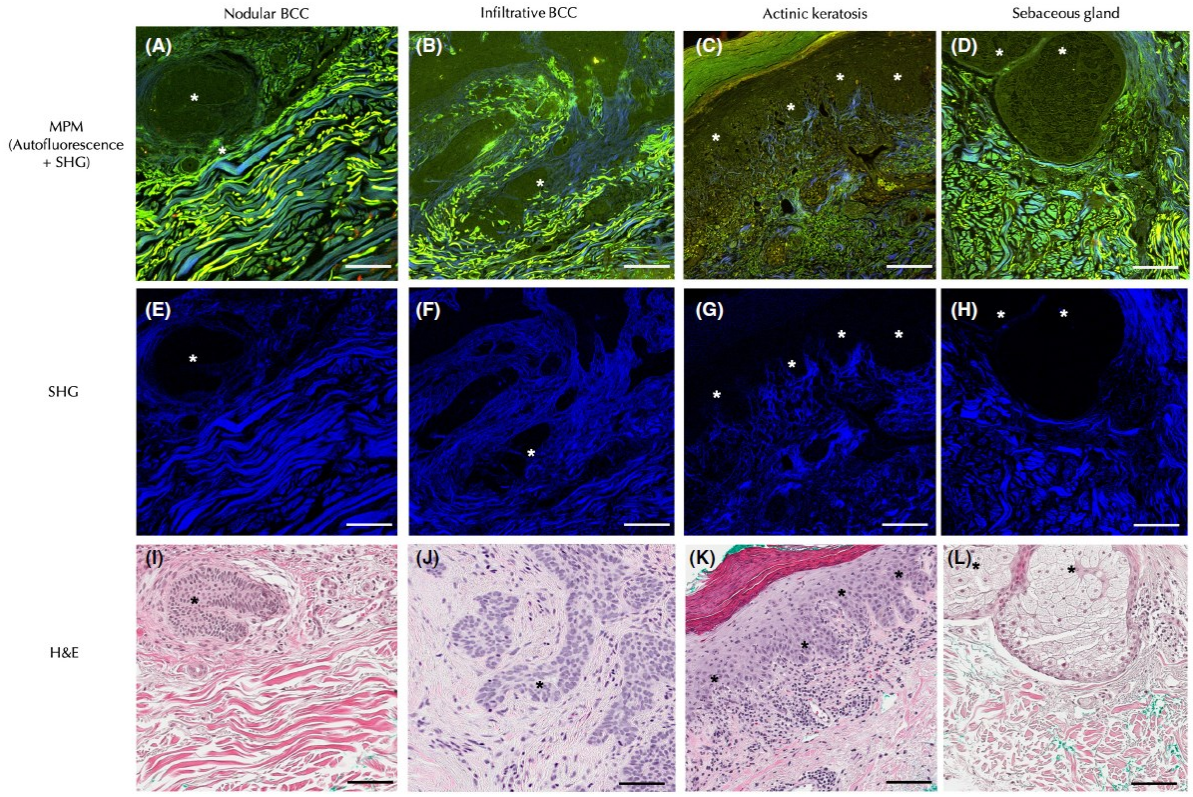

Figure 4 - *Representatives Multi Photon Microscopy (MPM) and corresponding H&E images used for analysis from (A) a nodular BCC, (B) an infiltrative BCC, (C) an actinic keratosis and (D) a sebaceous gland. (A–D). MPM images showing autofluorescence signals (colour-coded green/yellow/red) and SHG signal (colour-coded blue). (E–H) Isolated SHG images (colour-coded blue) used for collagen 1 quantification; (I–L) corresponding H&E images used as a map for MPM imaging. Asterisk shows features of interest in all the images. Note, due to absence of autofluorescence signal in panels (E–H), lesional areas appear dark and only type I collagen is seen (colour-coded blue). Scale bars: 100 μm. (CC-BY 4.0,* [25]*).*

1.2.3 Raman Spectroscopy

Raman spectroscopy is a fast, direct, and non-destructive technique that has various applications in different fields. It is used to identify molecules in a sample by measuring inelastic scattering of monochromatic light, which provides information about molecular vibrations. The Raman spectrum reflects the molecular composition of a sample [27]. Raman spectroscopy is widely used for in situ characterization of materials due to its label-free, non-invasive nature and high molecular specificity. It can provide molecular fingerprints and reveal various facets of material characterization, including biomolecular identification, solid-to-solid phase transitions, and spatial mapping of biomolecular species [28]. In the biomedical field, Raman spectroscopy has been used for diagnosing critical diseases such as cancers, infections, and neurodegenerative diseases.

Main applications:

- Identifying molecular constituents of tissues.
- Investigating chemical composition and structural changes.
- Studying biomolecules without the need for exogenous labels.

Raman spectroscopy is particularly useful for collagen studies because it can identify collagen-specific peaks, offering insights into collagen types, cross-linking, and structural modifications [22]. It is a non-destructive label-free technique applicable to intact tissues.

Raman spectroscopy has been used in recent studies to analyze collagen tissue. One study investigated the alterations in collagen types I and III in incisional hernia scars [29]. Another study focused on the detection of fibrosis in connective tissue using Raman microspectroscopy and imaging, which allowed for the discrimination of fibrotic and non-fibrotic collagen fibers [30]. Another study utilized Raman spectroscopy to analyze the conformational changes in collagen induced by burns, revealing structural changes and a shift in collagen secondary structure [31]. Raman spectroscopy has also been applied to characterize the extracellular matrix (ECM), including collagen, in various tissue systems, offering insights into tissue structure and composition (**Figure 5**) [32].

Recently, it has also been coupled with machine learning algorithms to differentiate healthy from artificially degraded articular cartilage and estimate its structural, compositional, and functional properties [33].

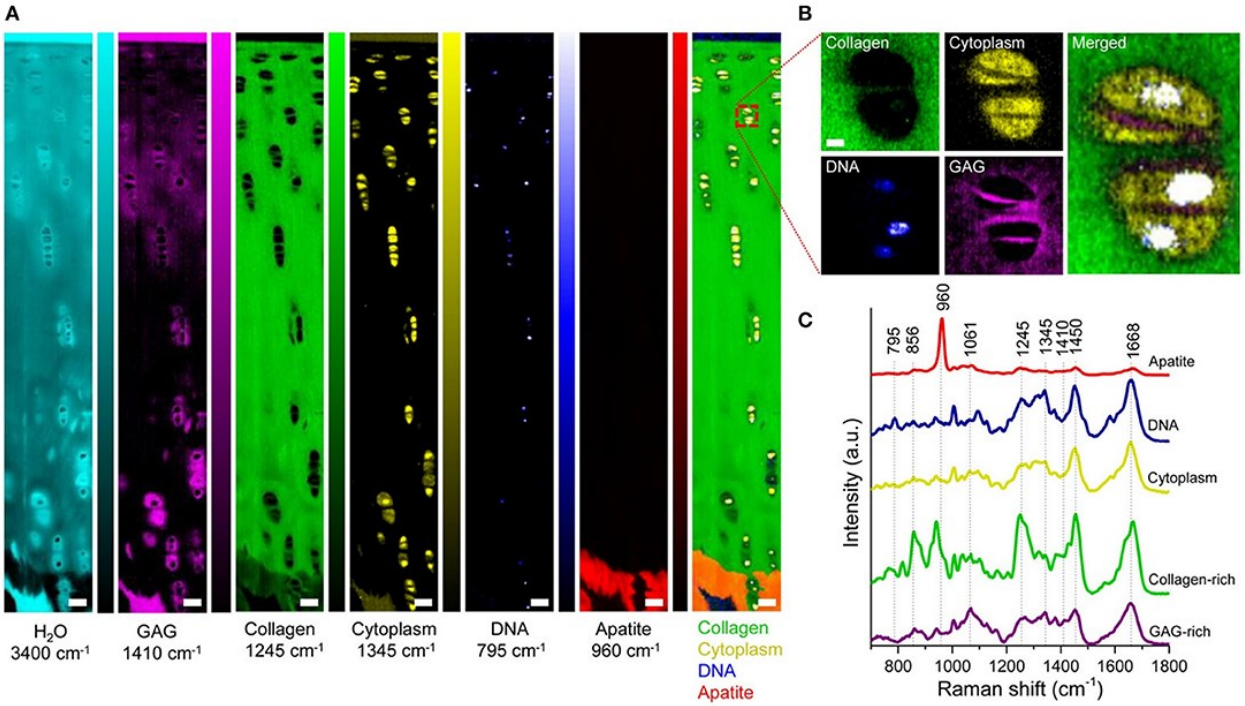

Figure 5 – *a) Univariate Raman spectroscopy images of articular cartilage showing the band intensity associated with H_2O, glycosaminoglycans, collagen, cytoplasm, DNA, apatite, and the overlay. Scale bar: 50 µm. b) High-resolution (≈ 0.3 µm) Raman spectroscopy image of chondrocytes and pericellular matrix obtained by imaging the glycosaminoglycans, cytoplasm, and DNA against collagen. Scale bar: 3 µm. c) Representative Raman spectra measured from articular cartilage with marked signatures for specific tissue components (*[32]*, CC-BY 4.0).*

1.2.4 Transmission Electron Microscopy

Transmission electron microscopy (TEM) is a technique that uses an electron beam to visualize samples at the micrometer to nanometer range. TEM works on the basis of imaging concepts, where an electron beam is concentrated onto a sample, creating an amplified image on a screen or film. TEM can achieve high-resolution imaging due to the short wavelength of electrons and the use of electromagnetic lenses for magnification. The scattering of incident electrons is utilized for image formation.

Main applications:

- Visualizing ultrastructural details of cells and tissues.
- Examining subcellular organelles, membranes, and macromolecular complexes.
- Investigating nanoscale structures and interactions.

TEM provides direct visualization of collagen fibrils at the nanoscale. It allows researchers to study collagen fibril diameter, arrangement, and interactions with other extracellular matrix components. TEM is instrumental in understanding the ultrastructure of collagen in various tissues. In recent years, Di Cecco et al. developed a novel liquid TEM approach to explore collagen mineralization in a liquid phase environment [34]. Rego et al. described a semi-automated image processing and statistical modeling pipeline for segmenting individual collagen fibrils from TEM images (**Figure 6**) [35]. Starborg et al. described a protocol for measuring collagen fibril diameter, volume fraction, length, cross-sectional shape, and 3D organization using TEM and serial block face-scanning electron microscopy [36].

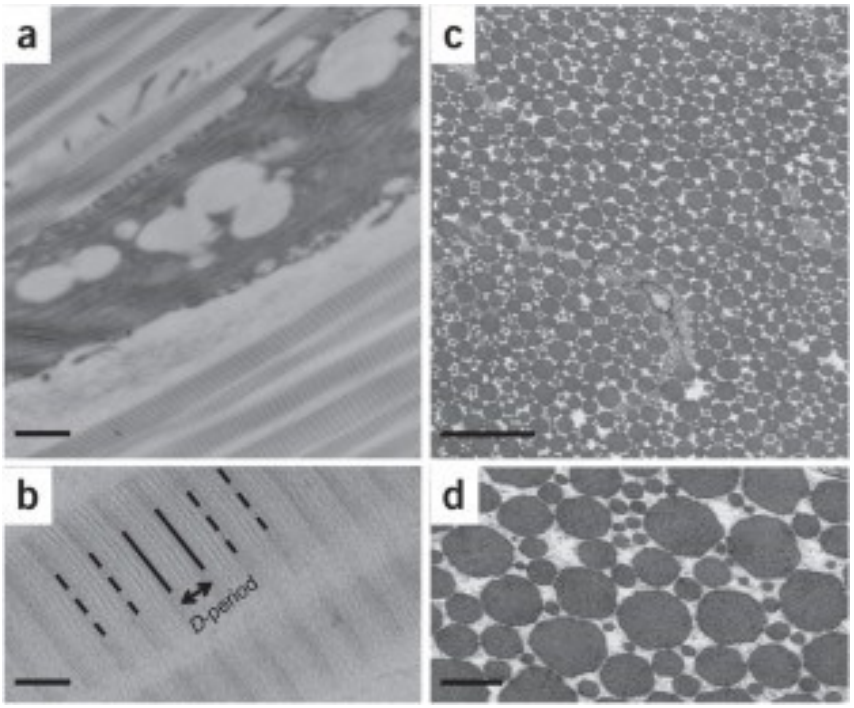

Figure 6 - *TEM of postnatal tendon. (a) A tendon fibroblast flanked by D-periodic collagen fibrils. Scale bar, 500 nm. (b) Enlarged view of (a) showing fibril D-periods. Scale bar, 100 nm. (c) Tendon sectioned transversely to the long axis of the tissue. Scale bar, 1 μm. (d) Enlarged view of (c) showing near-circularity of fibril profiles. Scale bar, 200 nm (Reproduced from [31], Springer Nature License nr. 5734670451870) .*

1.2.5 Optical Coherence Tomography

Optical coherence tomography (OCT) is based on the interference between light waves reflected by the reference and sample arms to obtain spatial information on tissue microstructure. This principle allows OCT to construct cross-sectional images of tissues in vivo [37]. OCT uses light in the near-infrared spectral range, which has a penetration depth of several hundred microns in tissue [38]. The backscattered light is measured with an interferometric setup to reconstruct the depth profile of the sample. The axial resolution and imaging range of an OCT system are determined by the characteristics of the light source and detector. OCT can be configured for various imaging applications, such as conventional microscopy, ophthalmic scanning, and endoscopy. The signal processing methods and algorithms in OCT make it sensitive to weak reflections and reveal functional information in addition to structure [39].

Main applications:

- Imaging biological tissues non-invasively and in real-time.
- Providing high-resolution, cross-sectional views of tissue microstructure.
- Monitoring structural changes in tissues over time.

OCT is highly relevant to collagen studies due to its ability to visualize tissue microstructure. In collagen-rich tissues, such as skin, tendons, and blood vessels, OCT can provide information on collagen fiber arrangement, density, and organization. Its non-invasive nature and ability to capture real-time images make it well-suited for studying collagen-rich tissues and monitoring dynamic processes. OCT complements other imaging techniques by providing detailed, in vivo information on tissue microstructure. Recent studies focused on collagen presented a variant of phase-resolved OCT for visualizing osmotically-induced strains in cartilaginous tissue impregnated with optical clearing agents (OCA) [40]. Another paper described a polarization-sensitive OCT (PS-OCT) system that can map collagen organization in vivo, demonstrating its ability to visualize myocardial architecture in rodent hearts and collagen structures responsible for skin tension lines in humans (**Figure 7**) [41]. A similar PS-OCT setup was used to

quantitatively determine the depth extent of thermal damage to the dermal collagen matrix in burn wounds [42]. Moreover, Lin et al., proposes a multimodal system combining polarization-sensitive OCT and second harmonic generation microscopy for examining collagen signatures in biological tissues [43]. Zyuryukina et al., used OCT to estimate the scattering coefficients of collagen bundles at different levels of tissue hydration, validating a theoretical model of collagen characteristics changing due to dehydration [44].

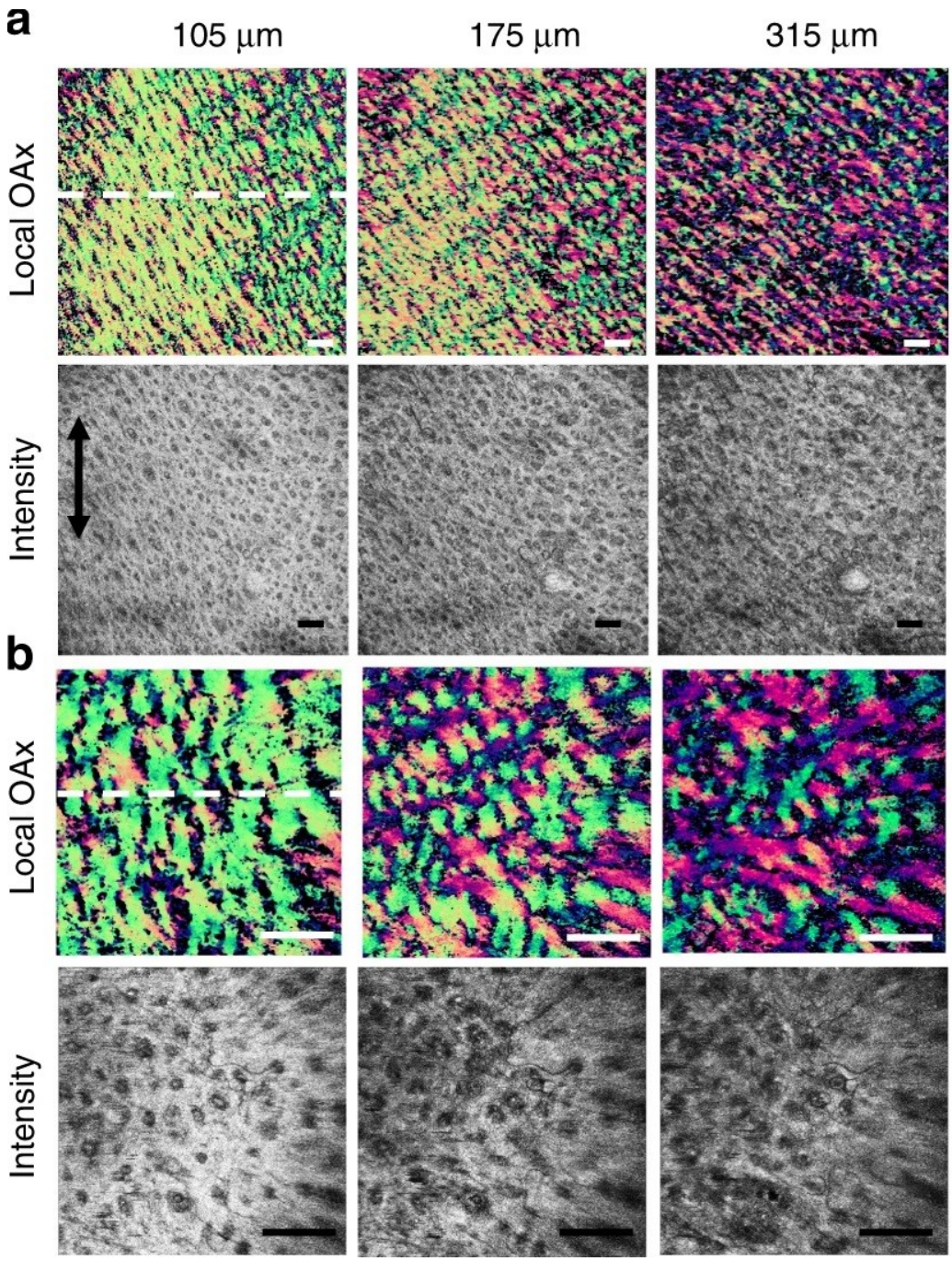

Figure 7 - *Depth-resolved collagen organizations within the cheek skin revealed by PS-OCT images. Results shown are obtained from a selected region of cheek skin. (a, b) The en-face local optical axis orientation (OAx) images and the corresponding en-face OCT intensity images at three different depths (105, 175, and 245 μm) using high and low lateral resolution scanning probe, respectively; Black double-headed arrow shows the direction of the body axis* ([41], *CC-BY 4.0).*

1.2.6 Phase-Contrast Micro Computed Tomography

Phase-Contrast Micro Computed Tomography (PC-μCT) is a form of X-ray computed tomography that exploits phase information in addition to attenuation. Traditional X-ray imaging relies on the absorption of X-rays, while phase-contrast imaging considers changes in the phase of X-rays as they pass through different materials. The phase of the waves travelling through the sample contributes to the modulation of the detected intensity in an X-ray phase-contrast imaging system [45].

Main applications:

- Visualizing soft tissues with improved contrast compared to conventional X-ray CT.
- Studying structural details and morphology without the need for contrast agents.
- Enabling high-resolution 3D imaging of biological samples.

PC-μCT is highly relevant to collagen studies as it excels in imaging soft tissues. It can provide detailed information about collagen fiber arrangement, distribution, and density in three dimensions. The technique is particularly valuable for non-destructive imaging of biological samples, allowing for the visualization of collagen structures without the need for staining or labeling. Recent studies took advantage of the technique for the quantification of cardiac collagen in a hypertensive rat model, and its correlation to heart failure, exploiting a neural network [46]. This imaging approach provides a unique potential for volumetric and highly detailed cartilage examination, being possible to visualize its defined intertwined three-layered organization as well as the wavy construction of the tidemark, which are the foundational elements of force distribution and biomechanical stability (**Figure 8**) [47].

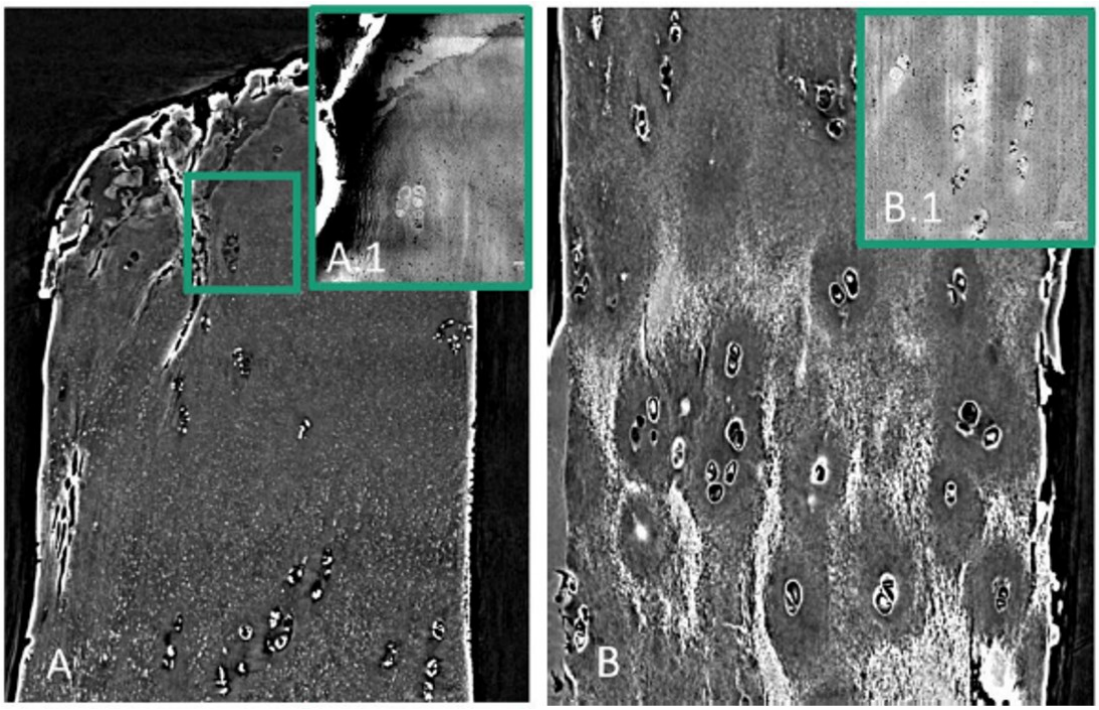

Figure 8 - *PC-μCT images from TOMCAT beamline (0.325 × 0.325 × 0.325 μm³ voxel size) of a degenerated cartilage sample (*[47]*, CC-BY 4.0).*

1.2.7 Integration and Complementary Use

Combining histology and TEM can provide both macroscopic and nanoscale information about tissue structure, although it requires careful consideration of sample preparation artifacts.

Raman spectroscopy complements histology by providing molecular details without the need for staining and can be applied to live tissues.

OCT offers real-time, in vivo imaging, making it suitable for dynamic studies and monitoring structural changes over time.

PC-μCT provides high-resolution 3D imaging of soft tissues, offering a non-destructive alternative to traditional absorption-based μCT.

By integrating these imaging techniques, researchers can obtain a multi-scale view of tissue structure, combining molecular, cellular, and tissue-level information. The choice

of techniques depends on the specific research question, the nature of the sample, and the desired spatial and temporal resolution. Collaboration among experts in different imaging modalities is often crucial for a comprehensive understanding of complex biological tissues.

For ease of understanding and for better visualization of the contexts of use and strengths of the techniques introduced, the main features are collected and presented in **Table 1**.

Table 1 – *Main features of the described imaging techniques: physical principle, main applications, strengths and weaknesses.*

Imaging Technique	Physical Principle	Main Applications	Strengths	Weaknesses
Histology	Microscopic examination of stained tissue sections.	- Visualizing tissue architecture. - Identifying different tissue types. - Assessing pathology.	- Excellent spatial resolution. - Specific stains highlight various tissue components.	- Invasive sample preparation may alter tissue morphology. - Limited 3D information.
Second Harmonic Generated Images (SHG)	Nonlinear optical process called second-harmonic generation.	- Collagen visualization	- High resolution - Selectively recognize collagen tissue	- Limited 3D information
Raman Spectroscopy	Measures molecular vibrations induced by laser light.	- Identifying molecular constituents of tissues. - Studying chemical composition.	- Provides molecular information without labels. - Applicable to intact tissues.	- Limited penetration depth. - Relatively slow imaging speed.
Transmission Electron Microscopy (TEM)	Uses electron beams for nanoscale imaging of internal structures.	- Visualizing ultrastructural details of cells and tissues.	- Extremely high spatial resolution at the nanoscale. - Direct visualization of	- Invasive sample preparation (fixation, thin sectioning).

Imaging Technique	Physical Principle	Main Applications	Strengths	Weaknesses
			subcellular structures.	- Limited field of view.
Optical Coherence Tomography (OCT)	Based on low-coherence interferometry, providing high-resolution cross-sectional images.	- Non-invasive imaging of tissue microstructure. - Real-time imaging. - In vivo applications.	- Real-time, non-invasive imaging. - High-resolution cross-sectional views.	- Limited penetration depth in highly scattering tissues. - Lower resolution compared to TEM.
Phase-Contrast Micro Computed Tomography (PC-µCT)	X-ray CT exploiting phase information for high-resolution 3D imaging.	- Visualizing soft tissues with high contrast. - Non-destructive 3D imaging.	- Non-destructive 3D imaging with high resolution. - Excellent contrast for soft tissues.	- Radiation exposure may limit live imaging. - Relatively lower resolution for nanoscale details.

2 Synchrotron Radiation Phase contrast High-resolution Tomography

Micro computed tomography (μCT) is a powerful imaging technique that utilizes X-rays to generate high-resolution 3D images of small objects or samples. Traditional μCT techniques primarily rely on absorption-based imaging, where the differences in X-ray attenuation are used to distinguish between different materials or structures within the sample.

PhC-μCT, because of the X-ray beam coherence, exploits experimental approaches not only based on the discrimination of the different attenuation properties of the elements composing the imaged object, but also dealing with phase-contrast between the phases inside it. The interaction of an object with x-rays, causes attenuation of the x-ray intensity and a change of the x-ray propagation direction by a refraction angle α. Conventional Tomography systems only record the x-ray intensity for each pixel in the detector, and so, can only measure the attenuation signal. The PhC-μCT system additionally records the local refraction angle α, which contains the information on the phase-shifting strength. Indeed, the complex refractive index is given by the equation:

$$n = 1 - \delta + i\beta \quad (1)$$

Away from absorption edges, and in the region where the photoelectric effect dominates absorption, δ and β can be expressed as functions of the electron density ρ and of the radiation wavelength λ in the following way:

$$\delta(\lambda) = \rho \frac{r_e \lambda^2}{2\pi} \quad (2)$$

$$\beta(\lambda) = \mu(\lambda) \frac{\lambda}{4\pi} \quad (3)$$

where r_e is the electron radius.

β is closely related to the linear attenuation coefficient μ visualized in conventional Tomography, and the phase-shifting strength is given by δ, real part of the index. Thus, the refraction angles depend on δ and, for x rays, are only of the order of $\alpha \approx 10^{-5}$ degrees.

The difficulty in measuring these minute angles was overcome with different setups, described in the following paragraphs [48], [49].

In the case of soft tissues imaging, as collagen is, the δ distribution reconstruction is more resolved than β, up to three order of magnitude superior, because the collagen components have similar electron densities respect surrounding extra-cellular matrix components; thus, δ contribution simplifies the image segmentation and the subsequent quantitative analysis of soft tissues.

Therefore, by exploiting phase information in Tomography, it is possible to enhance image contrast and improve the visualization of fine details, especially in samples with low X-Ray absorption contrast.

PhC-μCT techniques utilize phase retrieval methods to extract the phase information from the measured intensity data, in addition to the absorption information. By incorporating phase information into the reconstruction process, PhC-μCT can provide more detailed and accurate images, particularly for samples with subtle density variations or weakly absorbing materials. The phase information can reveal additional structural details, such as boundaries, interfaces, and internal features, that may not be clearly visible in absorption-based μCT images [50].

Various PhC-μCT methods have been developed since its first employment: Analyzer - based imaging (ABI), Grating interferometry and Propagation-based imaging (PBI) (**Figure 8**).

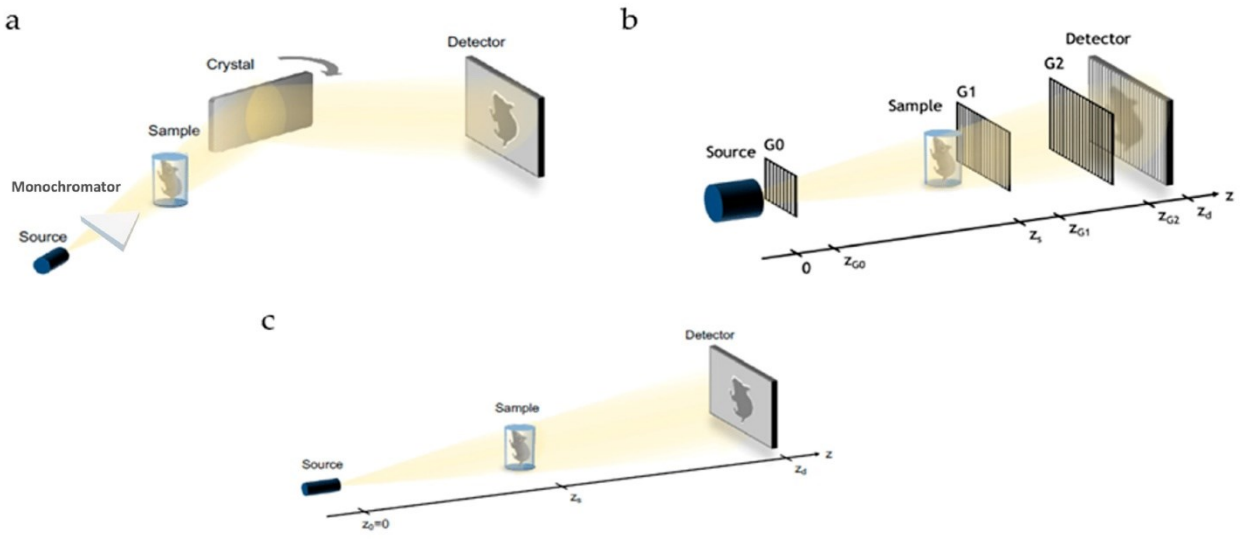

Figure 9 - *Schematics of most common phase-contrast setups: (a) analyzer-based, (b) grating interferometry, and (c) propagation-based. (*[50], *CC-BY 4.0)*

These techniques involve different approaches to phase retrieval and reconstruction, which can enhance the signal obtained in each setup.

The combination of PhC-μCT with advanced phase retrieval and reconstruction algorithms allows for improved imaging of biological samples, materials science, and other applications.

2.1 Analyzer-based imaging

Analyzer-based imaging (ABI) is a phase gradient-sensitive technique that uses highly selective analyzer crystals to filter the transmitted X-ray beam. The experimental setup for ABI entails the placement of a monochromator crystal preceding the sample and an analyzer crystal situated between the sample and the detector, according to the Bragg geometry. (**Figure 9a**). In the absence of a sample, if the analyzer crystal is aligned to the same angle as the crystal creating the monochromatic beam, all the monochromatic incoming X-rays are completely diffracted. However, in the presence of a sample, the analyzer crystal functions as an angular filter for the monochromatic radiation emitted by the sample. This phenomenon arises because the X-rays refracted by the sample exhibit varying angles of incidence upon reaching the analyzer crystal. Consequently, when these X-rays impinge upon the analyzer crystal, the Bragg diffraction condition is met only within a limited range of angles. In contrast, if the scattered or refracted X-rays possess incident angles falling outside this specified range, they remain unreflected and do not contribute to the signal. The manipulation of the analyzer crystal's tilt angle allows for the extraction of the refraction angle of the X-rays. Detectors commonly used are CCDs or CMOS, depending on the needs of the experiment and on the energy range of the radiation. ABI has several advantages, including its high sensitivity, low dose deposition to the sample, and the fact that it has been successfully implemented not only at synchrotrons but also with laboratory sources. However, it also has some

disadvantages, such as low beam stability (even at synchrotrons) and the need for long exposure times because of the low flux resulting after the monochromatization step. These characteristics make ABI a poor candidate for transfer to conventional laboratory-based X-ray sources, as demonstrated by the very few works that have been done in this direction. Further research is needed to address the challenges of beam stability and low flux to make ABI a more practical imaging modality [50].

2.2 Grating Interferometry

X-ray grating interferometry (GI) is a phase gradient-sensitive technique that uses gratings to create periodic interference patterns. The experimental setup for GI comprises two gratings, denoted as G1 and G2, a detector, and, in the case of a conventional X-ray source, an additional grating denoted as G0, which serves as a collimator to generate multiple small X-ray sources. Typically, G1 is designed as a phase grating, while G2 works as an absorption grating. G1 serves as in beam splitting, creating periodic interference patterns that vary with distance, referred to as the "Talbot carpet" (**Figure 9b**). This interference pattern arises from the waves emitted through G1 and manifests as periodic peaks of intensity at characteristic distances. The detector - in this setup also photon-counting pixel detectors could be found - is strategically positioned at one of these characteristic distances, typically where the intensity peaks are most pronounced. When a sample is introduced into the X-ray beam, these interference patterns become distorted due to various physical phenomena, including attenuation, refraction, and scattering. To extract valuable information from these distortions, an attenuation grating with the same periodicity as the original interference pattern is placed in front of the detector. This configuration translates the phase variations into intensity variations because the intensity peaks no longer align with the gaps between the bars of G2. To attain precise measurements of refraction angles and to characterize the attenuation and scattering properties, multiple acquisitions are conducted while adjusting the positions of the gratings. This comprehensive approach allows for the retrieval of detailed information regarding refraction, attenuation, and the scattering of X-rays, facilitating a more comprehensive analysis of the sample under investigation. GI has several

advantages, including its good sensitivity and the fact that it can be used with conventional X-ray sources. However, it also has some disadvantages, such as the need for complex and expensive experimental setups, especially for large fields of view. Furthermore, the acquisition time is still relatively long, and more studies are needed to reduce noise levels. Further research is needed to address the challenges of experimental setup complexity, acquisition time, and noise levels in order to make GI a more practical imaging modality [51].

2.3 Propagation-based imaging

Propagation-based imaging (PBI) is a phase gradient-sensitive technique that uses the spatial coherence of synchrotron X-rays to create interference patterns. The experimental configuration of PBI is similar to the conventional radiography one, with the only difference being that the distance between the detector and the sample depends on the desired level of spatial resolution (**Figure 9c**). When the X-rays pass through the sample, they are refracted by the different materials in the sample. This refraction causes the X-rays to interfere with each other, creating interference patterns. The occurrence of these interference patterns becomes increasingly pronounced as the separation distance between the sample and the CCD or CMOS detector is extended. These interference fringes manifest as alternating white and black lines that outline the contours of the sample. The phase of the X-rays can be retrieved from the interference fringes using a technique called phase retrieval. PBI has several advantages, including its simple experimental setup, rapid acquisition time, and relatively low noise levels. However, PBI also has some disadvantages: it is not as sensitive as other phase contrast imaging techniques, such as ABI. It is also not as well-suited for imaging large fields of view. It is the most widely used technique at synchrotrons, and it is becoming increasingly popular at laboratory sources.

It is necessary to retrieve the phase information to obtain the desired image: numerous techniques have been devised and refined globally for this purpose, yet the cornerstone among them is the widely recognized "Paganin method" [52]. This method relies upon

the application of the Transport of Intensity Equation (TIE), under the paraxial approximation, described by the following equation:

$$-k\frac{\partial I(\mathrm{x,y})}{\partial z} = \nabla_{\perp} \cdot [\mathrm{I(x,y)}\nabla_{\perp}\varphi(\mathrm{x,y})] \quad (4)$$

where k is the wave number $2\pi/\lambda$, x and y are the spatial coordinates in the plane perpendicular to the propagation axis z, I(x, y) and φ(x, y) are respectively, the intensity and the phase of the beam at the plane located at the propagation distance z and ∇ is gradient operator over the (x, y) plane. A comprehensive expansion of this equation, including its derivation and its application through various approaches, can be found in the highly detailed and well-crafted review authored by Zuo. et al. [53].

2.4 How the final image stack is achieved

Phase retrieval is a technique used in imaging to extract phase information from intensity measurements in order to reconstruct the phase contrast image. It allows for the recovery of the phase information, which contains valuable details about the object's structure and properties.

Phase retrieval is used in various fields, including X-ray imaging, electron microscopy, and optical imaging, to enhance image contrast and improve the visualization of fine details. In X-ray imaging, phase retrieval techniques can be used to distinguish between different types of tissues or materials based on their phase shifts.

Phase retrieval methods typically involve solving a mathematical problem to recover the phase information from the measured intensity data. This can be done using various algorithms.

One commonly used technique for phase retrieval is the Phase-Attenuation Duality (PAD) method, which is based on the relationship between phase and attenuation in the Fourier domain [54].

Another technique is the Contrast Transfer Function (CTF) method, which involves analyzing the intensity distribution of holograms to reconstruct the phase information [55].

One of the newest approaches in phase retrieval is the use of deep learning techniques, such as convolutional neural networks (CNNs), to directly learn the mapping between intensity measurements and phase information. These methods have shown promising results in terms of accuracy and speed [56]–[58].

Another recent approach is the use of ptychography, which involves scanning a focused beam over the sample and measuring the diffraction patterns. This allows for the retrieval of both amplitude and phase information, leading to improved reconstruction quality [59].

Non-linear phase-retrieval (NLPR) algorithms are also used, which avoid limiting approximations and result in sharp and accurate reconstructions [60], [61].

Once the phase information is retrieved, it is used to reconstruct the phase contrast image. Commonly used techniques for reconstruction include filtered back-projection and iterative algorithms. Filtered back-projection is a simple and fast technique that uses a Fourier-based filtering approach to reconstruct the image [62]. Iterative algorithms refine the reconstruction by minimizing a cost function based on the acquired data and the reconstructed image.

In terms of reconstruction, one of the newest approaches is the use of model-based iterative reconstruction (MBIR) algorithms. These algorithms incorporate prior knowledge about the object being imaged, such as its shape or material properties, to improve the quality of the reconstruction [63].

Finally, even in the reconstruction step, neural networks are apporting their contribution, being incorporated in filtered back propagation algorithms to make them more efficient [64] or developing a completely new paradigm in reconstruction [65], [66].

2.4.1 PyPhase collaboration

During my second year of the Doctoral Course, I had the chance to spend three months at the biomedical laboratory "Recherche Translationnelle et Innovation en Médecine et Complexité – TIMC", in collaboration with Université Grenoble Alpes (Grenoble, France).

In that visiting research experience, I could delve into phase retrieval algorithms implementation in PyPhase, an open-source Python package for phase retrieval from X-ray in-line phase contrast images (**Figure 10**) [67].

The aim of the package is to regroup a large number of phase retrieval algorithms to provide a toolbox for phase reconstructions for expert users. This permits the appropriate algorithm to be chosen for a specific imaging problem and facilitates quantitative comparison of algorithms. Another aim is to provide a platform for the development and implementation of phase retrieval algorithms. Finally, the package aims to simplify the access to phase contrast imaging by providing a simple interface for non-expert users.

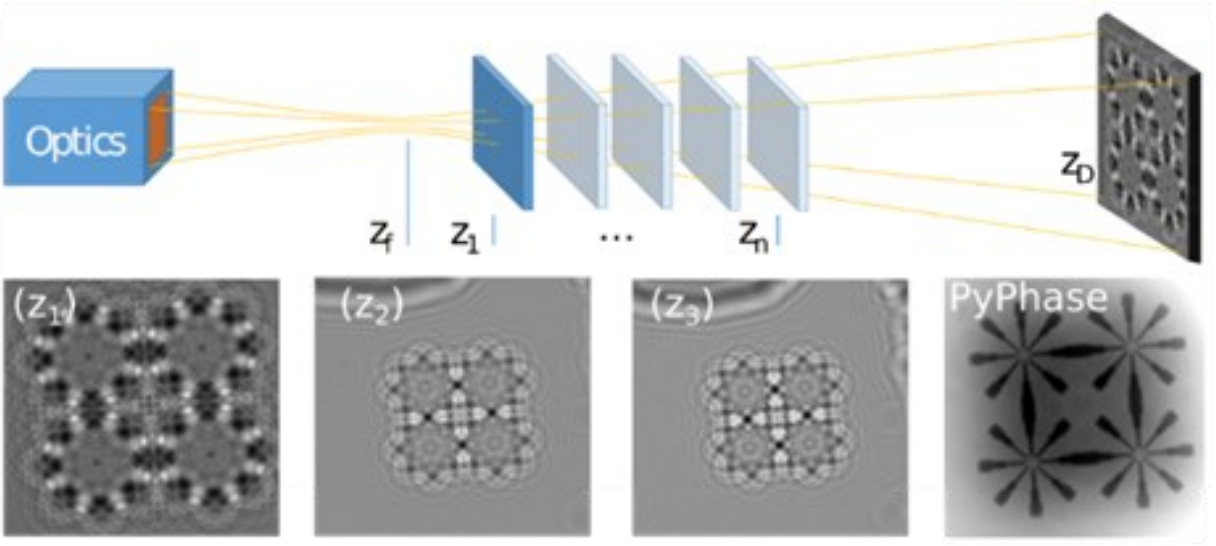

Figure 10 - *X-ray high-resolution imaging setup. Images at positions Z-n of the sample with respect to the detector ZD and focus position Zf yields different contrast and different magnifications. PyPhase reconstructs the phase and in some cases the attenuation from such images* [67].

In terms of functionality, the package is equipped with a *dataset module* that provides an interface to data from specific data sources - such as synchrotron beamlines - to facilitate routine use on large scale datasets. The *registrator module* contains algorithms for aligning

phase contrast images. The *propagator module* permits to simulate phase contrast images as well as provide the forward propagation step in iterative algorithms. The *parallelizer module* permits to parallelise reconstructions on different infrastructures.

My personal objective, during my scientific visit, was to widen the compatibility of the *dataset module*. As all our research on PhC-μCT took place at SYRMEP beamline (Elettra Synchrotron, Trieste), I implemented a new functionality to directly read SYRMEP file, in order to be able to take advantage of all the algorithms available in the package, even without any knowledge of how the information is stored inside the file (Appendix 1, for the whole package, please refer to: https://gitlab.in2p3.fr/mlanger/pyPhase).

2.5 SYRMEP beamline at Elettra Synchrotron

This whole thesis could not have existed if I had not had access to the Trieste Elettra Synchrotron's SYRMEP beamline. SYRMEP (SYnchrotron Radiation for MEdical Physics), as other beamlines at Elettra Synchrotron, allows for beamtime through a proposal procedure and consents access for a defined amount of time shifts of eight hours each.

During the Doctoral Course I accessed to it for a total of 27 shifts divided in 3 rounds, thanks to two winning proposal and an access granted through the EuroBioimaging circuit (visit https://www.eurobioimaging.eu/ for references).

In each experiment the same acquiring conditions were recreated, as the tissue under examination had the same collagenous matrix. In particular, paraffin-embedded soft tissues samples were analyzed.

At SYRMEP beamline it is possible to work in both conditions of absorption and/or phase contrast; our purpose was soft tissue imaging so the latter was adopted (**Figure 11**).

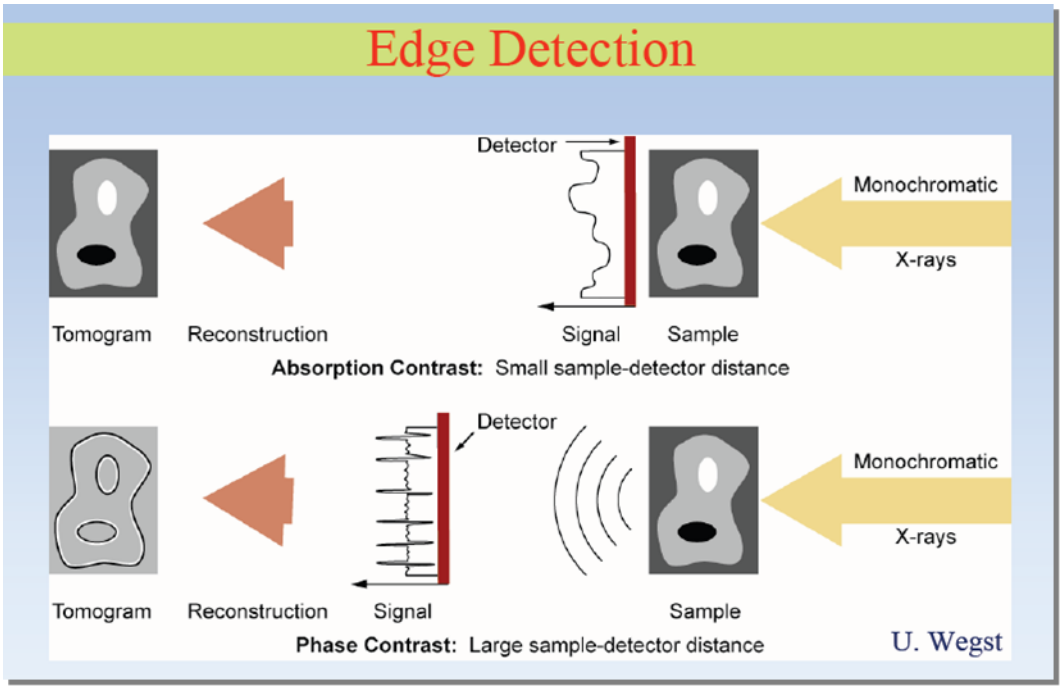

Figure 11 – *Schematics of the dual modality for absorption and phase contrast. In our experiment a white beam was employed.*

The aim of the setting employed was to obtain the highest resolution achievable at the beamline, 0.89 μm, to meet the dimensional scale of collagen fibrils and fibers (Figure 1). To do so, with the support of the SYRMEP team, iteratively the sample-detector distance was adjusted, ending with a distance of 10 cm (Figure 12). At the same way, an appropriate filter was selected, 0.5 mm Silicon filter, obtaining a white beam with peak energy value of 17 keV.

Accordingly with these settings parameters, an exposure time of 200 ms was set for each step of the acquisition. The scanning itself was performed with an incremental angle of 0.1° on a total rotation of 180°, for a total of 1800 projections. The frame of acquisition was set to 2048x2048 pixels, resulting in a reconstructed volume of about 6 mm3. Those samples with a vertical dimension greater than the field of view of the frame, were acquired with multiple scanning in sequence, at different z positions, allowing the acquisition of the whole sample. After the acquisition, each sample volume was immediately reconstructed using the STP software (SYRMEP Tomo Project), an open source software made available from the beamline team, with an user friendly interface

which helps users to go through the whole process of phase-retrieval and reconstruction, setting the suitable parameters for each sample.

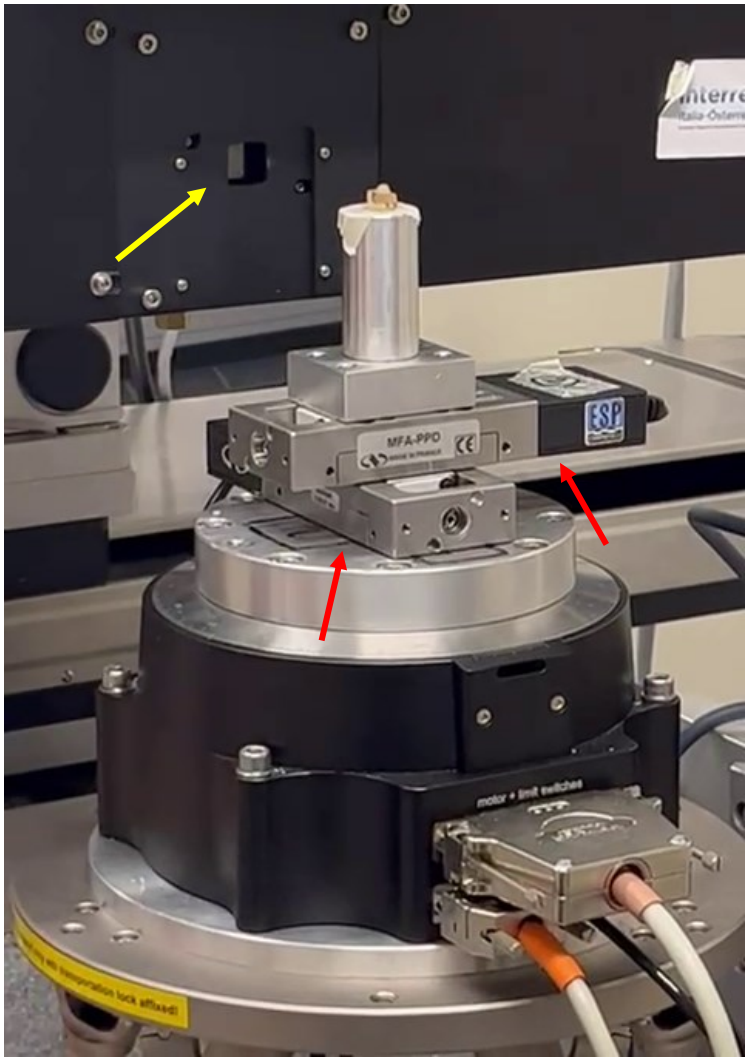

Figure 12 – *Picture taken at the SYRMEP beamline: sample installed on its support, prior to the tomographic acquisition routine. In the picture it is possible to recognize the detector, the small spot in front of the sample (yellow arrow), and the motorized remote control for the perfective movements in x and y directions (red arrows), to accurately position the sample within the field of view.*

3 Results obtained during the Doctoral Course

In the following paragraphs, the main results obtained during the Doctoral Course will be presented: many of them were already published in peer reviewed journals of international distribution, some of them are still under review.

The utilization of Synchrotron Radiation High Resolution Tomography has yielded exciting outcomes across all various domains in which it has been employed. It is noteworthy that the capability to operate within diverse contexts and to integrate this 3D imaging modality alongside other techniques already prevalent in biomedical research represents a significant achievement. The conception of interdisciplinary studies aimed at offering novel insights into physiology and pathology, while leveraging innovative techniques, has been highly challenging and formative.

Nevertheless, this thesis will exclusively present results pertaining to synchrotron tomography applied to collagen-based tissues, suitably contextualized, in alignment with its aim.

3.1 Animal model study of Rare Diseases: lung fibrosis in a murine model of scleroderma

This study was the result of a multidisciplinary collaboration between several research groups: namely, the Department of Clinical and Molecular Sciences and the Department of Odontostomatologic and Specialized Clinical Sciences of the Marche Polytechnic University, the Animal Breeding and Testing Service, Scientific Technological Centre, Institute for Scientific Hospitalization and Care (IRCCS) - National Institute for Hospitalization and Care of the Elderly (INRCA) in Falconara (AN), the Department of Medical Sciences of the University of Torino and the Department of Internal Medicine of the Marche University Hospital. The full manuscript is not yet published but is under review at the journal Science Translational Medicine.

- *Background of the study*:

Systemic sclerosis (SSc), also known as scleroderma, is a multi-organ fibrotic disease of unknown etiology [68]. Fibrosis, characterized by the disruption of normal tissue architecture and resultant organ dysfunction, constitutes the primary clinical manifestation of the illness, significantly impacting prognosis. Notably, lung involvement stands as the leading cause of mortality among SSc patients.[69]. The pathogenesis of SSc fibrosis is complex, involving various factors, notably an aberrant immune response directed towards cellular targets. Similar to other fibrotic conditions, a central event in the development of SSc fibrosis is the trans-differentiation of local fibroblasts into profibrotic myofibroblasts [70].

Several studies highlighted the role of the Platelet Derived Growth Factor (PDGF)/PDGF Receptor (PDGFR) pathway in the activation of profibrotic myofibroblasts [71]. Human PDGFRα (HuPDGFRα) is also one of the targets of the autoimmune response in SSc [72].

Intradermal injection of two different stimulatory HuPDGFRα monoclonal antibodies (mAbs) (*VH$_{PAM}$-V$_k$16F4* and *VH$_{PAM}$-V$_\lambda$16F4*, alone or in mixture) in normal human skin equivalents grafted onto the back of Severe combined immunodeficient (SCID) mice resulted in enhanced collagen deposition in the dermis, increased fibroblast activation markers and vascular alterations, leading to scleroderma-like skin fibrosis. In order to replicate these findings in vivo, a novel humanized mouse model of SSc fibrosis was created through the generation of an immunocompetent transgenic mouse with ubiquitous expression of human PDGFRα. In this novel transgenic mouse tissue fibrosis was induced via transfer of HuPDGFRα mAbs.

- *Synchrotron Radiation Phase Contrast High Resolution Tomography application:*

We used this method to investigate the mice lung 3D morphology and the alveolar physical density distribution in the retrieved biopsies.

Scans were performed using the following settings: ELETTRA operating parameters of 2GeV and 300 mA; X-rays filtered by 0.5 mm Silicon and with an average energy of 17 keV; exposure time per projection set to 0.2 seconds, collecting 1800 projections over a

total range of 180°; the sample-detector distance was set to 100 mm with a pixel size of 890 nm.

The SYRMEP Tomo Project (STP) open source software was run to achieve the tomographic reconstructions [73], exploiting the Paganin's method [52] by setting, after some tests, the δ/β ratio to 100.

The commercial software VG Studio MAX 1.2 (Volume Graphics, vers. 1.2.1, Heidelberg, Germany) was used to generate 2D and 3D images as well as to evaluate the thickness distribution of the different structures (bronchioles, vessels and alveoli) by the Wall Thickness Analysis add-on module.

Afterwards, the BoneJ Plugin of the NIH ImageJ software, version 3 [74], was used to evaluate the following parameters in alveolar portions: the mean alveolar wall thickness (Th, expressed in micrometers), the mean alveolar wall spacing (Sp, expressed in micrometers) and the alveolar volume density (VD, expressed as a percentage). Moreover, we investigated the alveoli shape and 3D complexity by using a morphometric descriptor of their interconnectivity, namely the alveolar connectivity density (Conn.D, expressed in $pixel^{-3}$), and the overall alveolar fractal dimension (FD). Conn.D is a complexity parameter with higher values for better-connected tissue structures and lower values for poorly connected ones. Furthermore, the fractal dimension parameter is a complexity index describing at which extent an irregular structure tends to fill space at different scales [75]. We used the box-counting dimension with the following settings: starting box size (px): 28; smallest box size (px): 6; box scaling factor: 1.2; grid translations: 0.

Moreover, being the reconstructed complex refractive index linearly related to the mass physical density (PD), this parameter was calculated within the overall alveolar volumetric domain. The absolute values of the PD (expressed in g/cm^3) could not be retrieved because the reconstructed complex refractive index might be biased by the chosen δ/β ratio used in the Paganin phase retrieval processing. However, being the investigated samples comparable in terms of size and composition, the mass density differences between the groups of study within the alveolar portion of the biopsies translated into different mean values of the tissue peak in the gray-level scale (8 bit, 0-

255). This post-processing calculation of the PD parameter was performed using the PeakFit software (Systat Software, San Jose, CA, USA).

- *Results*:

Following 28 days of HuPDGFRα mAbs administration, histological examination of skin samples revealed marked skin thickening and dermal fibrosis (data not shown). In order to investigate the thickening of lung structures, a three-dimensional (3D) approach was necessary, as through histology the quantification of the differences in fibrotic deposition was not consistent (histologic quantitative data not shown).

Notably, 3D analysis revealed the deposition of collagen fibers not only around lung bronchioles and vasculature (**Figure 13**) but also on the alveolar walls, which exhibited marked thickening, as described by the parameters taken into account (**Figure 14**). Indeed, both Alveolar wall Thickness and Spacing (respectively their thickness and the mean distance between two adjacent walls) were significantly different with respect to the control PBS treatment in all the combinations of mAbs, leading to a reduction of the alveolar space. The mean Alveolar Volume Density increased, resulting in an overall stiffening of the structures, testified also by an increasing of the Alveolar Physical Density. All these parameters pointed to a fibrotic response of lung tissues. However, the formation of new fibrotic connections among alveoli was not observed; indeed, Connectivity Density of alveolar structures did not show any significative differences despite the reduced alveolar space. This implies there has not been an augmented complexity of the 3D architecture of the structure, possibly due to the insufficient duration of HuPDGFRα mAbs administration.

Overall, interestingly, examination of lung structure by synchrotron imaging revealed significant interstitial lung fibrosis confirming that the generated novel humanized mouse model is not only effective in reproducing skin fibrosis but also in reproducing lung fibrosis. This is of paramount interest because this humanized mouse model may be useful to identify and validate new therapeutic strategies for SSc and other diseases.

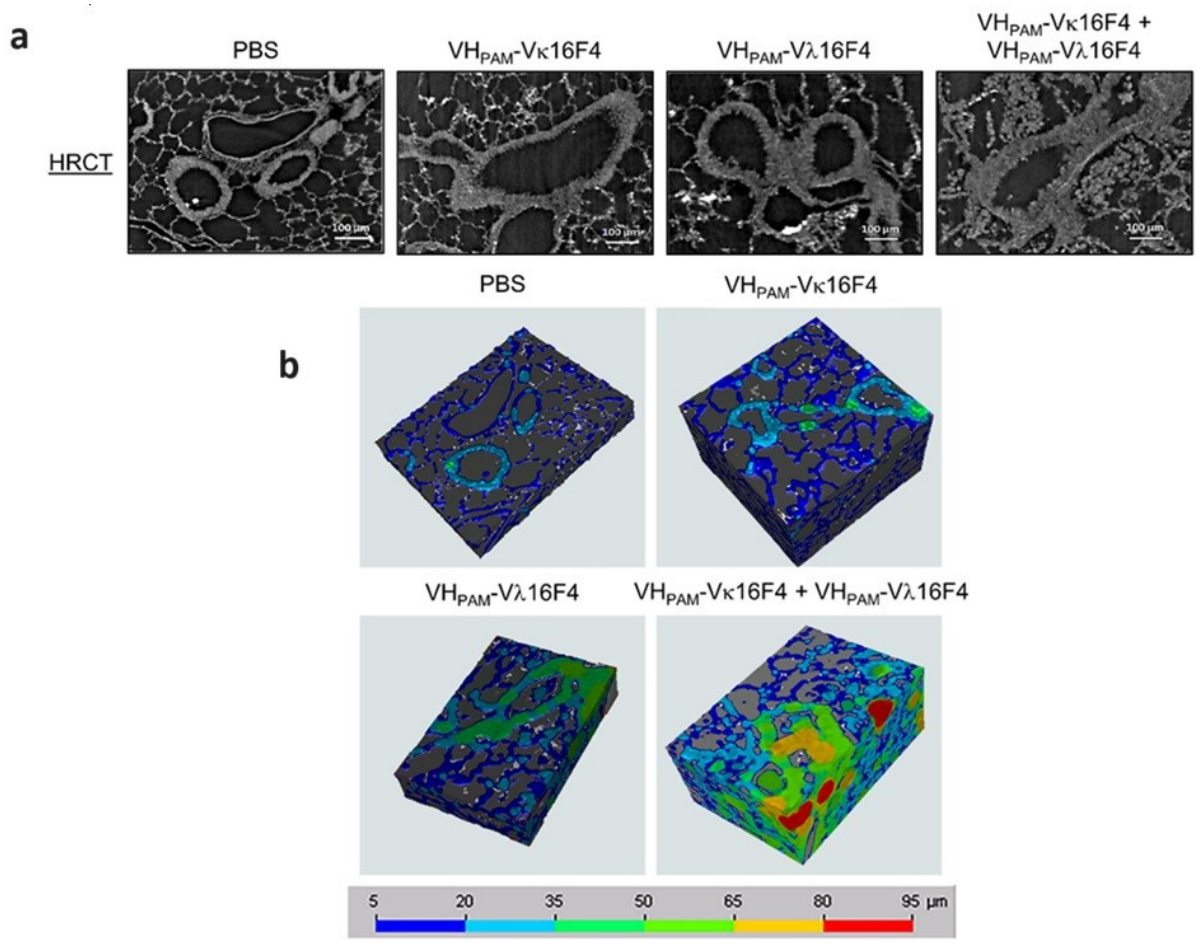

Figure 13 - *(**a**) Synchrotron-based high-resolution computed tomography (HRCT) of lung sections obtained at day 28 administration of stimulatory HuPDGFRα mAbs (VHPAM-Vκ16F4 or VHPAM-Vλ16F4), either alone or in mixture, resulted in increased deposition of collagen fibers around lung bronchioles and vasculature as compared to vehicle control (PBS); (**b**) Synchrotron-based high-resolution 3D tomographic reconstruction of lung volumes obtained at day 28. Thickness color maps (bottom scale) of lung representative 3D reconstructions confirmed the induction of peribronchiolar and perivascular pulmonary fibrosis following mAb challenging in comparison with vehicle control (PBS).*

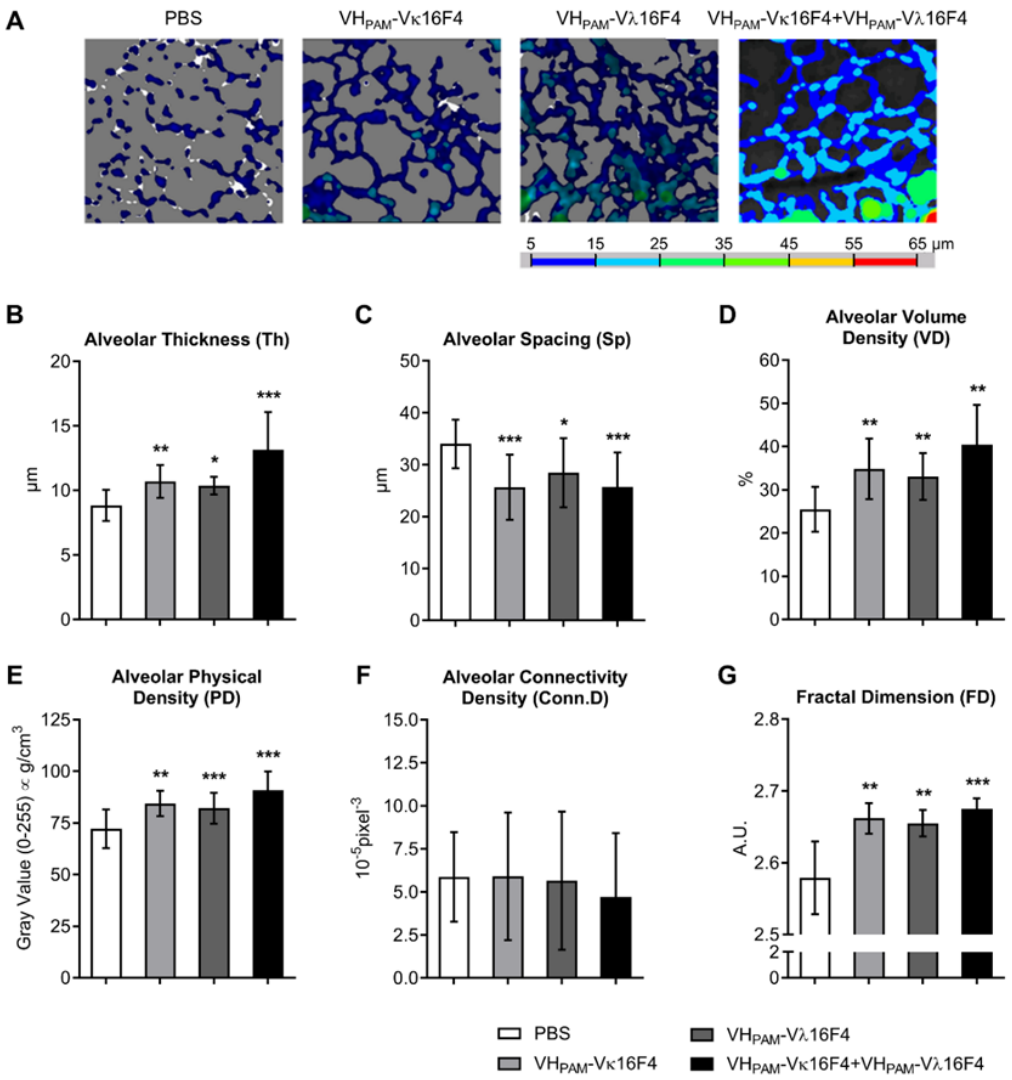

Figure 14 - *Induction of alveolar lung fibrosis by continuous subcutaneous administration of HuPDGFRα mAbs.* ***(A)*** *Synchrotron-based high-resolution computed tomography (HRCT) of lung alveolar tissue sections obtained on day 28 from C57BL/6-huPDGFRα transgenic mice (n=8 per group) that received the aforementioned treatments. Thickness color maps showed an increased deposition of collagen fibers in the lung alveolar walls following mice treatment with stimulatory HuPDGFRα mAbs VHPAM-Vk16F4 or VHPAM-Vλ16F4, either alone or in mixture, as compared to vehicle control (PBS). Representative images of three independent experiments are shown. Statistical analysis of the following parameters, as measured by Synchrotron-based HRCT in the alveolar portions of the lungs:* ***(B)*** *alveolar walls thickness (Th - µm);* ***(C)*** *alveolar walls spacing (Sp - µm);* ***(D)*** *alveolar wall specific volume (VD - %);* ***(E)*** *alveolar wall physical density (PD – grey level (0-255) ∝ g/cm³);* ***(F)*** *alveolar wall connectivity density (Conn.D – pixel⁻³) and* ***(G)*** *Fractal Dimension (FD). Results are mean ± SD. * = P < 0.05 compared to PBS-treated mice. ** = P < 0.01 compared to PBS-treated mice. *** = P < 0.001 compared to PBS-treated mice.*

3.2 Human studies

The extensive introduction focused on collagen characteristics and functions (Chapter 1), should have convinced that collagen tissues' elasto-mechanic role bonds it to the morphology of the site it is extracted from, which could weaken the results coming from animal experimentations.

Indeed, extrapolating findings from animal models to human studies, may not always be straightforward. Variations in species, genetic backgrounds, environmental factors (including biomechanical ones), and experimental conditions can all influence collagen behavior and complicate the interpretation of results.

Owing to the progress in imaging methodologies, the utilization of human biopsy specimens extends beyond diagnostic purposes. Tissue-specific characteristics of collagen, resulting in variety and complexity, suggest that the investigation of its behavior, in both physiological and pathological conditions, requires the effort of gathering human samples, which provide a guarantee of the reliability of the results obtained.

3.2.1 Gynecology: uterine leiomyoma

Also this study, as the previous on animal models described in Paragraph 3.1, was the result of a multidisciplinary collaboration between several research groups: namely, the Department of Odontostomatologic and Specialized Clinical Sciences, the Department of Life and Environmental Sciences and the Department of Experimental and Clinical Medicine of the Marche Polytechnic University. Moreover, this study directly involved also scientists of the Elettra-Sincrotrone Trieste S.C.p.A.

- *Background of the study*:

Uterine leiomyoma, also known as uterine fibroid, is a complex area of study in terms of its precise pathogenesis. Although the exact mechanisms have not been fully elucidated,

several factors have been shown to be implicated in its development: these include genetic alterations, epigenetic mechanisms, hormonal influences (such as steroids), growth factors, cytokines, and chemokines [76], [77]. Leiomyomas exhibit inflammatory and fibrotic characteristics, contributing to significant morbidity and potentially impacting women's health, fertility, and pregnancy outcomes [78]. This condition, prevalent among women of reproductive age, ranks as one of the most common benign uterine neoplasms. It typically involves an impairment in collagen production and manifests as smooth muscle tumors originating from the myometrium [79].

It is believed that uterine fibroids arise from the activation of myofibroblasts and subsequent production of extracellular matrix (ECM) within the myometrium. This process may be triggered by various factors, including inflammation and hormonal imbalances. However, the specific sequence of events and the interplay between these factors in initiating and promoting leiomyoma growth are still under investigation. Thus, uterine leiomyoma could serve as a valuable model for understanding pathological alterations of the extracellular matrix (ECM) with special reference to the collagen-based component.

The aim of the study was to evaluate a multimodal analytical approach that integrates 2D and 3D high-resolution techniques to investigate both the microstructural organization and the secondary structure of collagen [73]. This investigation focuses on intramural uterine leiomyoma samples through ex-vivo analysis at the tissue level. The methodology combines Phase-Contrast High-Resolution Tomography and Fourier Transform Infrared Imaging spectroscopy along with optical and trasmission electron microscopies. Additionally, the sensitivity of this multidisciplinary approach is assessed by analyzing leiomyoma samples treated ex vivo with targeted supplements, such as eicosapentaenoic (EPA) and docosahexaenoic (DHA) omega-3 fatty acids, known to modulate collagen signaling.

From five patients, aged from 40 to 46, samples were collected in intramural position. Leiomyoma biopsies and surrounding myometrium tissue were extracted. Some portions were treated with EPA and DHA 50 μM (Sigma-Aldrich) for 48 h, other portions used as controls, were maintained under the same conditions without any treatment (NT) (**Figure 15**).

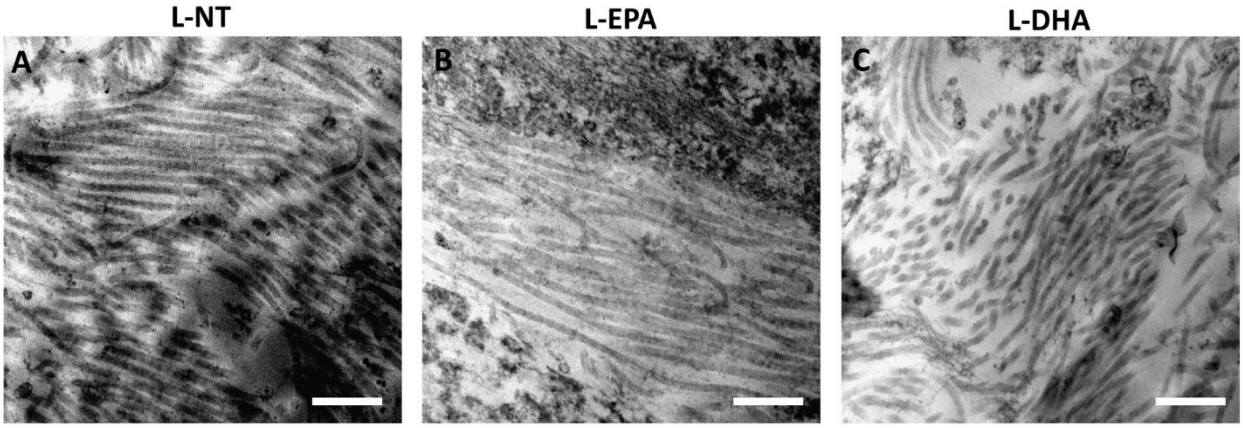

Figure 15 - *Representative TEM images of leiomyoma samples: (A) not treated (L-NT) and treated with (B) EPA (L-EPA) and (C) DHA (L-DHA). Scale bars: 400 nm* [79].

- *Synchrotron Radiation Phase Contrast High Resolution Tomography application*:

The experiments were conducted at the ELETTRA Synchrotron Radiation Facility in Basovizza, Italy, using paraffin-embedded samples.

Phase-contrast imaging was employed to enhance image contrast by reconstructing the δ distribution, which facilitated segmentation and quantitative analysis of grey-level histograms. The scans were performed using the beam provided by the ELETTRA facility (2 GeV, 300 mA), filtered by 0.5 mm silicon, with an average energy of 19 keV. The exposure time per projection was set to 0.2 s, with 1800 projections collected over a total range of 180°. The sample-detector distance was 100 mm, resulting in a pixel size of 890 nm.

Tomographic reconstruction was carried out using the SYRMEP Tomo Project (STP) open-source software [73], applying Paganin's method to retrieve the phase contrast signal and reconstruct the refractive index decrement δ [52]. The δ/β ratio was set to 100, assuming a linear relationship between the absorption index β and the refractive index decrement δ.

Subsequently, NIH ImageJ software was utilized to generate stacks of 2D images, where grey levels corresponded to the phase distribution. The Mixture Modeling algorithm was

employed to threshold and segment the histograms. Several 2D slices from each biopsy were analyzed to achieve complete sample mapping.

For each biopsy, several 2D-slices were analyzed: each of them was fully included in the sample bulk and the complete set of them allowed achieving the complete sample mapping. Quantitative analysis was conducted in two steps.

To start, collagen-specific amount (Coll/TOT, expressed as a percentage) was evaluated in each biopsy, for both myometrial (M) and leiomyoma (L) tissues in each condition: not treated (M-NT and L-NT), as well as biopsies treated with EPA and DHA for 48 hours (M-EPA, L-EPA, M-DHA, and L-DHA). The evaluation of this parameter allowed to quantify the collagen amount respect to the total tissue amount in each biopsy.

In the second step, representative biopsies were selected for full 3D morphometric analysis, evaluating parameters such as collagen-specific volume (CollV/TV), mean collagen bundle thickness (CollTh), mean collagen bundle number (CollNr), and mean collagen bundle spacing (CollSp). Additionally, collagen bundle shape and 3D complexity were studied using morphometric descriptors for the interconnectivity and orientation of collagen bundles. The connectivity density (Conn.D - pixel-3) was assessed, with high values indicating better-connected collagen bundles, characteristic of more entangled fibrotic tissues, while low values suggest well-oriented functional bundles. Along with Connectivity Density, the collagen anisotropy degree index (DA) was calculated to measure the similarity of a structure to a uniform distribution. It ranges between 0, indicating perfect isotropy, and 1, representing collagen bundles confined to a single plane or axis. Moreover, fractal theory was applied to quantify collagen structures through the fractal dimension, which indicates the extent to which an irregular structure fills space at different scales. The box-counting dimension method was utilized for its easy implementation, with specific settings including a starting box size (px) of 48, smallest box size (px) of 6, box scaling factor of 1.2, and no grid translations. The comprehensive morphometric analysis, encompassing collagen bundle shape and 3D complexity, was conducted using the BoneJ Plugin of the ImageJ software, version 3 [74].

The statistical analysis of morphometric data was performed with the software package SigmaStat 3.5 (Systat, San Jose, CA). Statistical significance among NT, EPA and DHA

treatments was performed using one-way ANOVA and Holm-Sidak multiple comparisons test; statistical significance between L and M samples in each treatment was evaluated by Student's t-test. Statistical significance was set at $p < 0.05$.

- *Results*:

Starting with a visual analysis (**Figure 16-A**), the M-NT samples exhibited well-oriented collagen bundles, with consistent spacing between bundles predominantly occupied by smooth muscle tissues. In contrast, the L-NT samples showed thicker and more interconnected collagen bundles, resulting in a globally more isotropic morphology compared to M-NT. Regarding treatments, no significant changes were observed in M-EPA samples compared to M-NT. However, L-EPA biopsies displayed intermediate morphological characteristics between M-NT/M-EPA and L-NT samples, with a higher number of collagen bundles respect to the myometrium samples but showing a better organization than L-NT samples. This first result shows how myometrium was little or not at all affected by the fatty acid treatment, while in leiomyoma the collagen signaling impairment was more effective (**Figure 16A**).

To compare the relative amount of collagen in myometrium (M) and leiomyoma (L) samples, before and after EPA and DHA treatments, the COLL/TOT ratio was calculated. Statistical analysis revealed higher collagen amounts in L-NT compared to M-NT; a statistically significant decrease in collagen amount in L-EPA and L-DHA compared to L-NT; no significant changes between M-NT and M-EPA or M-DHA (**Figure 16-C**).

Notably, higher standard deviations were observed in L-EPA and L-DHA samples than in the other groups, potentially due to variations in biopsy dimensions. Specifically, smaller samples exhibited lower average collagen values following EPA treatment compared to larger samples, where bulk portions were not reached by the treatment.

Additionally, the analysis indicated that the EPA treatment penetrated the tissue to a maximum depth of approximately 500 μm. This depth was visualized in representative M-EPA biopsies, where green spots corresponding to residual blood clots were observed, providing insights into the penetration thickness of the EPA treatment (**Figure 16–B**).

Furthermore, DHA treatment appeared to induce structural damage in both myometrium (M-DHA) and leiomyoma (L-DHA) samples.

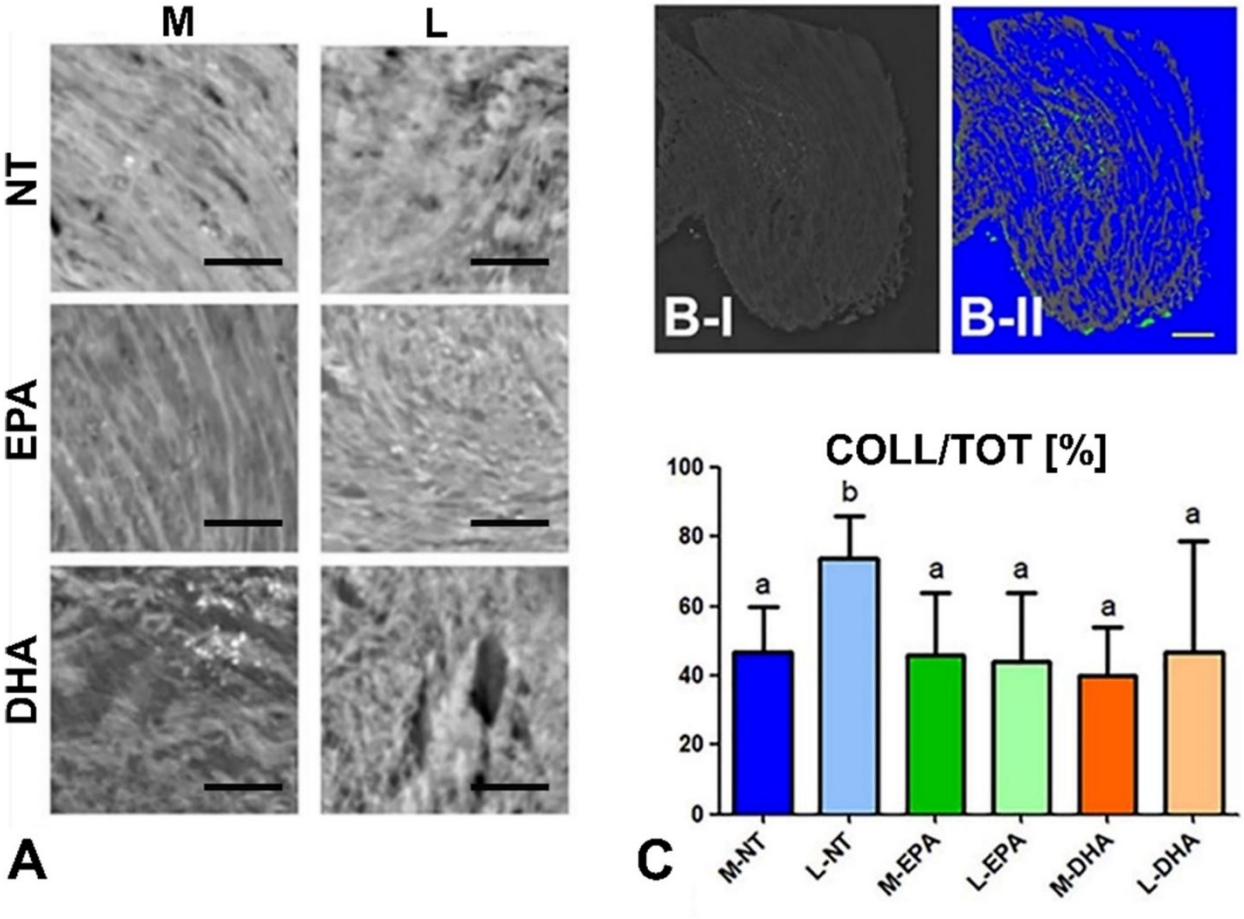

Figure 16 - *(A) Representative PhC-microCT sections of myometrium (M) and leiomyoma (L) samples, before (M-NT and L-NT) and after EPA (M-EPA and L-EPA) and DHA (M-DHA and L-DHA) treatments showing the morphological distribution of collagen bundles (light grey) (bars: 50 μm). (B-I) Representative PhC-microCT section of myometrium after EPA treatment (M-EPA) and (B-II) the corresponding false color image showing the morphological distribution of collagen bundles (light grey) and blood clots residuals (green spots) (yellow bar: 200 μm). (C) Histograms showing the numerical variation of COLL/TOT (%), as evaluated by PhC-microCT morphometric analysis on myometrium (M) and leiomyoma (L) samples, not treated (NT) and after EPA and DHA treatments. Data are presented as mean ± SD. Different letters over histograms indicate statistically significant differences among groups (One-way ANOVA Holm-Sidak multiple comparisons test). Statistical significance was set at $p < 0.05$* [79].

To proceed with a comprehensive 3D morphometric analysis, a single patient has been chosen as representative. Numerous stack sequences of 2D axial slices (sub-volumes, each with a final volume of 180 × 180 × 150 μm^3), covering the entire biopsies, were examined and morphometrically analyzed (**Figure 17**).

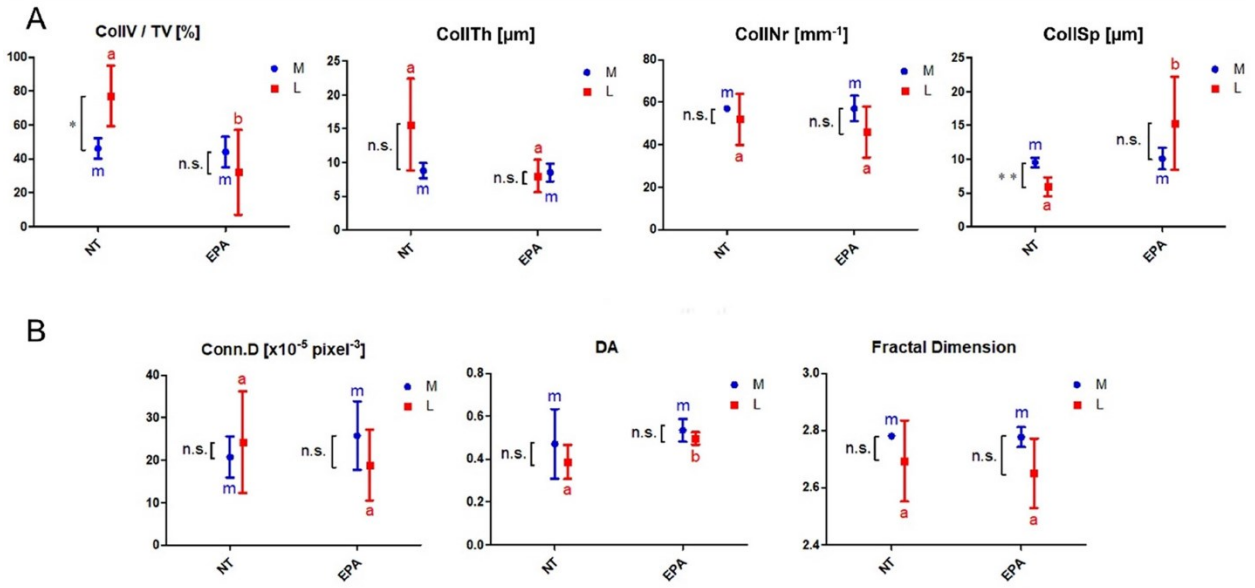

Figure 17 - *Statistical analysis of PhC-microCT morphometric parameters. (A) Specific collagen volume (CollV/TV - %); mean collagen bundles thickness (CollTh - µm); mean collagen bundles number (CollNr – mm^{-1}), and mean collagen bundles spacing (CollSp - µm). (B) Shape and 3D complexity study: connectivity density (Conn.D – $pixel^{-3}$); collagen anisotropy degree index (DA), and Fractal Dimension. Data are presented as mean ± SD. Different letters indicate statistically significant differences among NT and EPA treated samples, while asterisks indicate statistically significant differences between myometrium and leiomyoma in each treatment (Student's t-test). *p < 0.05; **p < 0.01 [73].*

Consistently with a previous study [77], the collagen bundle specific volume (CollV/TV) was notably higher in leiomyoma (L-NT) compared to healthy myometrium (M-NT). Conversely, the mean distance between collagen bundles (CollSp) in L-NT was significantly lower than in M-NT. These morphometric findings support the increased rigidity of the pathological tissue (L-NT) compared to the healthy tissue (M-NT), aligning with observations made through optical microscopy (data not shown) and corroborated by previous literature.

Additionally, it's noteworthy that while EPA treatment did not lead to significant changes in any of the studied morphometric parameters in healthy myometrium (M-EPA), in leiomyoma samples (L-EPA), EPA induced a considerable reduction in collagen bundle specific volume (CollV/TV) and a significant increase in both the mean distance between collagen bundles (CollSp) and the degree of anisotropy (DA). This parameter

demonstrated a statistically significant increase in anisotropy in the pathological tissues treated with EPA compared to the untreated ones, indicating a restoration of the functional orientation of the collagen bundles. Frequently associated with the degree of anisotropy, connectivity density analysis, which assesses the number of connections between structures per unit volume, revealed in leiomyoma samples a slightly higher average number of connections between collagen bundles, which decreased after EPA treatment. Moreover, no significant difference was observed between M-EPA and L-EPA for any of the analyzed morphometric parameters.

These morphometric findings suggest promising outcomes regarding the potential role of EPA in fibroid treatment, indicating a reduction in the rigidity of pathological tissue. Furthermore, despite a comparable number of analyzed samples, the standard deviations of data obtained for pathological tissues (L) were consistently higher than for healthy myometrium (M), highlighting significant structural heterogeneity within leiomyoma tissues.

Beside all these morphological findings obtained by synchrotron-based PhC-microCT, this study excelled in demonstrating the potential of combining high resolution techniques for a comprehensive characterization of collagen tissues.

3.2.2 Dentistry: peri-implant connective tissue

As in previous preclinical (Paragraph 3.1) and clinical cases (Paragraph 3.2.1), also the present investigation was the result of a multidisciplinary collaboration between different research groups: namely, the Department of Odontostomatologic and Specialized Clinical Sciences of the Marche Polytechnic University, the Department of Medical, Oral and Biotechnological Sciences of the University of Chieti-Pescara, and the Unit of Prosthodontics and Implant Prosthodontics of the Department of Surgical Sciences (DISC), University of Genova. Also for this study, there was a direct involvement of Elettra-Sincrotrone research scientists. Moreover, I acknowledge Euro-BioImaging (www.eurobioimaging.eu) for providing access to imaging technologies and services via the PCI @ Italy – Phase Contrast Imaging Flagship Node Trieste (Trieste, Italy) -

experiment PID: 1611. Finally, I acknowledge Sweden & Martina for providing all dental implants studied in this investigation.

- *Background of the study*:

The distinction between the periodontal connective tissue and implant-connective tissue interface is widely recognized, characterized by varying arrangements of collagen fibers surrounding the implant [80]. However, Romanos et al. study, as well as subsequent ones, examined the connective tissue surrounding implant abutments predominantly relying on two-dimensional investigations, particularly histological evaluations. Their results were concordant on observing circular fibers, along with fibers aligned parallel to the longitudinal axis of the implant, in apico-coronal direction. Only in some reports, fibers have been noted to insert onto the implant surface also in radial direction [81], [82]. However, all these studies agreed in stating that symmetrically formed and orderly connective tissues surrounding the implant neck could prevent inflammatory cell migration to the apex and, consequently, avoiding bone resorption and implant failure.

Soft tissues around implants develop during the wound-healing process. After implant placement, mucosa heals by forming an epithelium and adapting the connective tissue to the implant surface [83].

In this framework, X-ray phase-contrast imaging was here used, for the first time to my best knowledge, to study the 3D organization of connective tissue around the abutments (1st experiment) and shed light on its morphological architecture, also making hypotheses about how physical forces drive this biological response during the wound-healing process.

Beyond the comprehension of the 3D organization, a subsequent study (2nd experiment) was conducted to assess the impact of different shaped implants on the healing process. Evaluations were made simplifying the compared geometries to a straight profile, with convergent or divergent vertical shapes. Thus, the directionality of the normal forces exerted by and on the collagen bundles is the only responsible of differences observed among samples (**Figure 18**).

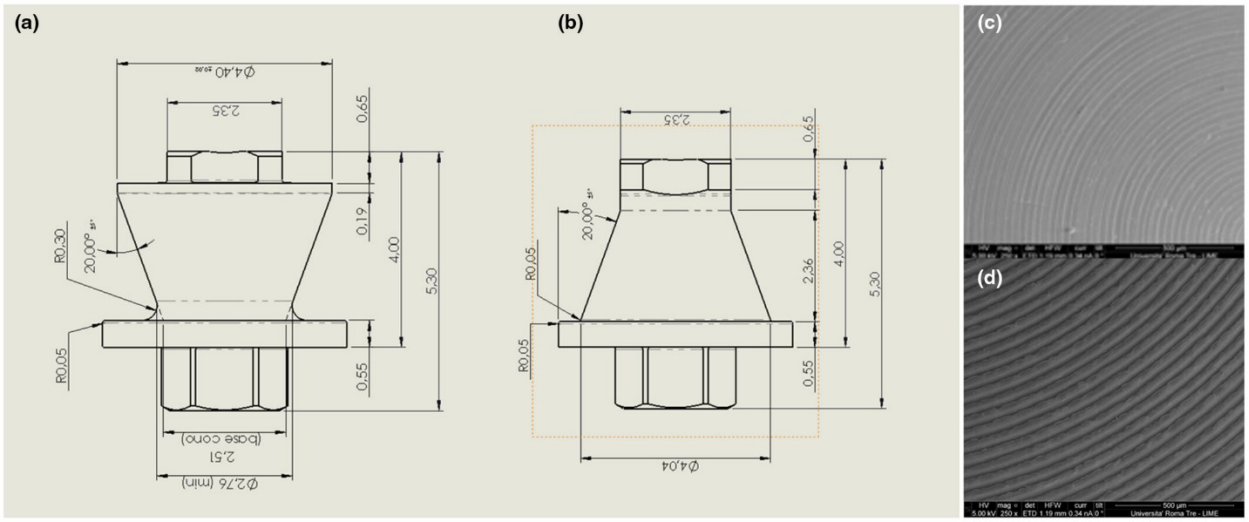

Figure 18 - *Schematic draw of the different macro-designs: (a) divergent, (b) convergent. SEM images of the different surfaced included in the study; (c) smooth, MAC; (d) tridimensional, UTM. Courtesy Sweden & Martina (*[84]*, CC-BY 4.0).*

The convergent geometry also presented a variation in the surficial pattern, with a micro-grooved geometry, resulting in three groups: DIV-MAC (divergent-machined), CONV-MAC (convergent-machined) and CONV-UTM (convergent-ultrathin threaded micro-surface) (**Figure 18-d**).

All biopsies - abutments with surrounding soft tissues -, after explantation from a patient, were fixed in 10% buffered formalin, then dehydrated in a graded series of ethanol rinses, and finally embedded in a glycolmethacrylate resin (Methyl-Methacrylate [MMA] following chemical dehydration). After polymerization, the abutments embedded in resin blocks were sectioned along their longitudinal axis in order to obtain two portions (portions 1 and 2 in **Figure 19)**. Portion 1 was handled by traditional methods and cut with Precise 1 (Automated System; Assing). The tissue/abutment half incorporated in resin and intended for synchrotron analysis (portion 2 in **Figure 19**) was mounted in a clamp and subsequently viewed under microscope (Leica Wild M3Z Stereo Zoom Microscope) to highlight the soft tissue/abutment interface. Subsequently, a thin scalpel was inserted into the interface; afterwards, through a lever action, the abutment was detached from the block.

Figure 19 - *Abutments surrounded by soft tissues and embedded in resin blocks were sectioned along their longitudinal axis in order to obtain two portions. Portion 1 was used to obtain the longitudinal sections to the major axis of the abutment; afterwards, the sample slices were stained by toluidine blue and acid fuchsin. Portion 2 was examined by synchrotron radiation imaging, after removal of the abutment; afterwards, it was sectioned along its transversal axis for evaluation under a polarized light microscope (*[84], *CC-BY 4.0).*

- *Synchrotron Radiation Phase Contrast High Resolution Tomography application*:

The PhC-microCT scanning (for both the 1st and the 2nd experiments) were conducted at the SYRMEP beamline of the ELETTRA Synchrotron Facility in Basovizza, TS, Italy.

The scans of the 1st experiment were performed using the pink beam delivered by the synchrotron facility, filtered by a 0.5-mm thick silicon plate, resulting in an X-ray beam with an average energy of 19 keV. Exposure time per projection was set to 0.2 s over a total range of 180 degrees, with a sample-detector distance of 100 mm, yielding an 890 nm isotropic pixel size. Tomographic reconstruction was accomplished using the SYRMEP Tomo Project (STP) software [73], employing Paganin's method for phase retrieval to reconstruct the refractive index decrement [52].

Quantitative analysis of the 3D microarchitecture of collagen bundles involved contrast enhancement followed by median filtering to homogenize the collagen signal and reduce

noise. Subsequently, a threshold was applied to isolate the collagen-phase signal for analysis.

Following reconstruction, 3D images and sequences of longitudinal and transversal 2D slices were generated using VG Studio MAX 1.2, ORS Dragonfly 2024.1 (non-commercial license) and ImageJ software [74].

For the 2nd experiment, the same setting was maintained for Synchrotron acquisition. Moreover, similarly to the 1st experiment, for each biopsy, a longitudinal sequence of subvolumes was investigated, from the apical location to the margin of the peri-implant mucosa; each subvolume had a fixed dimension of 540 × 270 × 270 μm^3 and was oriented with the longest side as close as possible to the interface with the abutment.

- *Results*:

Starting with the first study (1st experiment), the biopsies exhibited an organized arrangement of collagen bundles, showing circular collagen bundles (C-CB), that were transversal to the vertical axis of the implant, and longitudinal collagen bundles (L-CB). Notably, no radial collagen fibers were observed with respect to the implant surface. Circular fibers were predominant and were close to the interface with the implant. Longitudinal fibers, on the other hand, were situated internally, intertwining with circular bundles. Additionally, a few blood vessels were detected in both transversal and longitudinal planes (**Figure 20** and **Figure 21**).

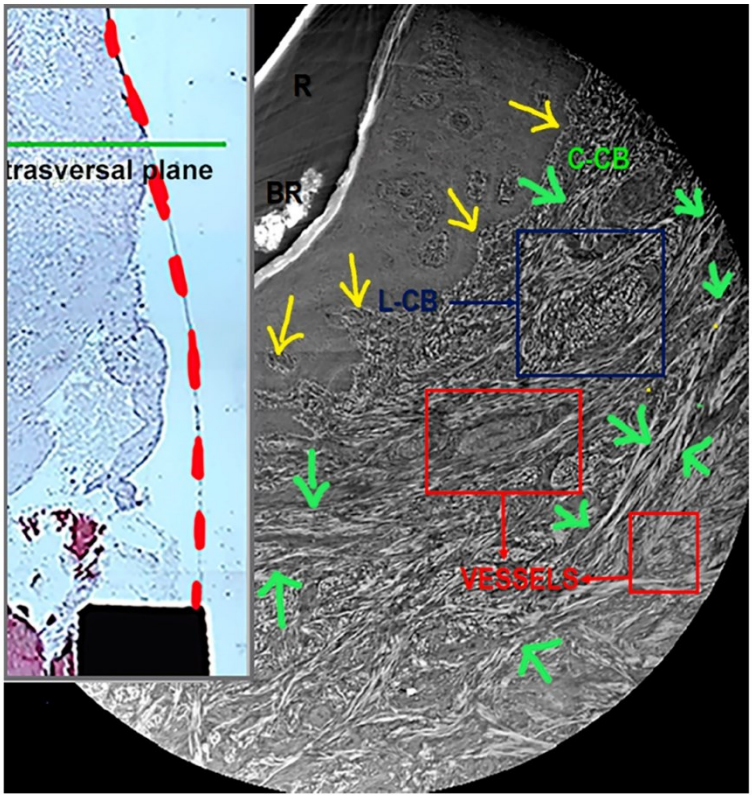

Figure 20 - *Synchrotron radiation-based phase-contrast microtomography in the junctional epithelium portion (JEP): transversal 2D slice in a sampling plane, as indicated (green line) in the top-left insert. Red dashed line: abutment interface before removal. Circular collagen bundles (C-CB) are indicated by the green arrows, with evidence of interlaced longitudinal collagen bundles (L-CB) and few vessels. Yellow arrows show the interface between connective tissue (CT) and junctional epithelium (JE). BR: bone residuals; R: resin* ([85], *CC-BY 4.0).*

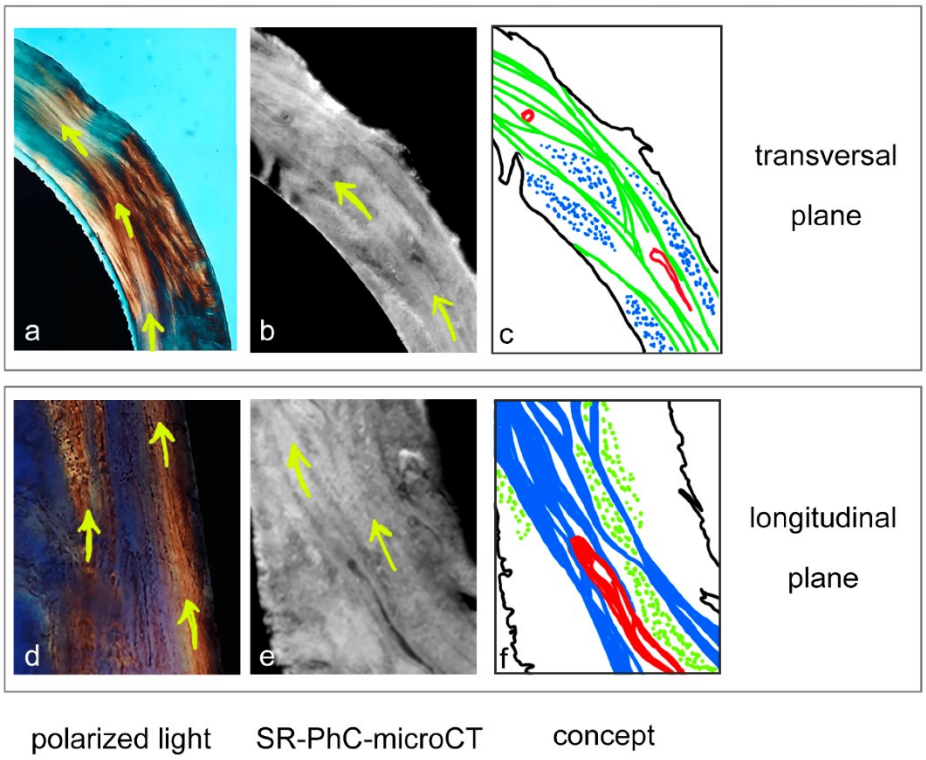

Figure 21 - *Polarized light and synchrotron-based microtomography in the connective tissue portion: from the combined imaging to the concept. (**a**,**d**) Polarized light evidence: (**a**) transversal section of the peri-implant soft tissue in the coronal portion of the implant: the pale yellow color indicated the collagen fibers that run circularly around the implant (yellow arrows), whereas the blue color showed the collagen fibers parallel to the long axis of the implant; (**d**) longitudinal section of the peri-implant soft tissue in the coronal portion of the implant: the junctional epithelium was in close contact with the implant surface. No inflammatory infiltrate was observed. Yellow color represented the collagen fibers parallel to the long axis of the implant–abutment (yellow arrows), whereas the blue color showed the collagen fibers that run to the long axis of the implant (circularly around the implant–abutment unit); (**b**–**e**) synchrotron radiation-based phase-contrast microtomography: (**b**) sampling 2D slice in a transversal plane; (**e**) sampling of a 2D slice in a longitudinal plane; (**c**) concept drawing describing structures in the panel-b slice: circular collagen bundles (green lines), with evidence of interlaced longitudinal collagen bundles (blue spots) and few vessels (red structures); **(f)** concept drawing describing structures in panel-e slice: longitudinal collagen bundles (blue lines) with evidence of interlaced circular collagen bundles (green spots) and few vessels (red structures)* ([85], *CC-BY 4.0).*

For the second study (2nd experiment), assessed to verify if the implant macro- and micro-geometry can promote a better healing response in the surrounding connective tissues, a set of parameters were quantified and compared using appropriate statistical tools.

In particular, four parameters were extracted: connective tissue height (Conn.Tissue Height – expressed in mm); connective tissue-specific volume (Conn.Tissue SpV – expressed in %); connective tissue degree of anisotropy (Conn.Tissue DA); and connective tissue connectivity density (Conn.Tissue ConnD –expressed in $pixel^{-3}$). The Conn.Tissue Height is the vertical distance that was measured in a direction that was parallel to the long axis of the abutment; the Conn.Tissue SpV is the ratio between the collagen voxels volume and the total volume of the investigated tissue; the Conn.Tissue DA measures the similarity of a structure to a uniform distribution. Finally, the Conn.Tissue ConnD is a morphometric descriptor for the interconnectivity of the collagen bundles: higher values correspond to better-connected collagen bundles, i.e. more entangled peri-implant connective tissues.

Descriptive statistics and differences between experimental groups were analyzed using the software package Prism 6.0 (GraphPad Software). The null hypothesis of no difference between groups was rejected at $p < .05$. Data distributions of the 2nd experiment were checked for normality by Kolmogorov–Smirnov and Shapiro–Wilk tests, homogeneity of variances by Levene test. The parameters showing normality and homogeneity of variance between groups were evaluated using one-way ANOVA and Tukey's multiple comparisons test; otherwise, the groups were tested using the nonparametric Kruskal–Wallis one-way ANOVA on Ranks and Dunn's multiple comparisons test.

Full biopsies were investigated for each patient obtaining 3D-imaging and morphometric mapping of the whole peri-implant connective tissue in the three experimental groups: namely, DIV-MAC (divergent-machined), CONV-MAC (convergent-machined) and CONV-UTM (convergent-ultrathin threaded micro-surface).

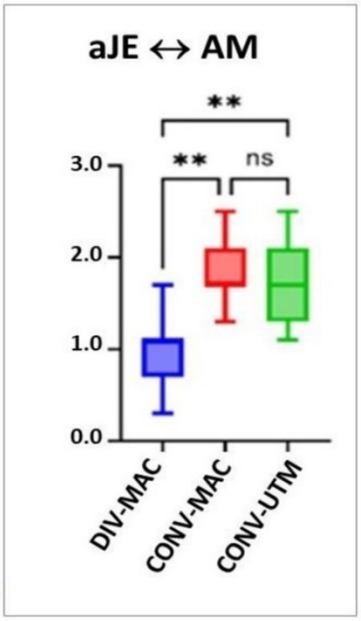

Figure 22 - *3D Synchrotron morphometric evaluation of the connective portion (apical extension of the junctional epithelium (aJE), and the apical location of the abutment (AM), aJE ↔ AM). Comparisons between the three experimental groups (i.e., DIV-MAC, CONV-MAC, CONV-UTM). Upper and lower ends of boxes represent 75th and 25th percentiles. The median value is showed with a solid line. *p < .05, **p < .01 (*[84], *CC-BY 4.0).*

The height (axial direction of the implant) of the peri-implant connective tissue (Conn.Tissue height – mm) was measured in the area closest to the interface with the abutment, that is, within a radial maximum distance from the interface of about 300–400 μm. These results are reported in **Figure 22**. The one-way ANOVA test, applied because normality and homogeneity of variances were verified, showed differences among the three experimental groups (**Table 2**). In particular, Tukey's multiple comparisons test indicated differences between the DIV-MAC group and both CONV-MAC and CONV-UTM groups, with significantly higher values for these last two groups.

Table 2 – *PhC-microCT parameters in peri-implant connective tissues of the three experimental groups ([84], CC-BY 4.0)*

Parameter	DIV-MAC[a]	CONV-MAC[a]	CONV-UTM[a]	*p*
Conn.Tissue height (mm)	**1.0 ± 0.1, 1.1**	**1.8 ± 0.1, 1.7**	**1.7 ± 0.2, 1.7**	.0009[b]
Conn.Tissue SpV (%)	**84 ± 3, 84**	**88 ± 2, 88**	**94 ± 1, 95**	.0180[c]
Conn.Tissue DA	0.55 ± 0.07, 0.57	0.51 ± 0.05, 0.54	0.55 ± 0.05, 0.54	.8299[b]
Conn.Tissue ConnD ($\times 10^{-3}$ px^{-3})	1.8 ± 0.2, 1.8	2.1 ± 0.2, 2.1	2.5 ± 0.1, 2.4	.0533[b]
Multiple comparisons tests				
Groups	**Parameters**	**Mean**		***p***
DIV-MAC vs. CONV-MAC	Conn.Tissue height (mm)	**1.0 vs. 1.8**		.0013[d]
DIV-MAC vs. CONV-UTM		**1.0 vs. 1.7**		.0053[d]
CONV-MAC vs. CONV-UTM		1.8 vs. 1.7		.8269[d]
DIV-MAC vs. CONV-MAC	Conn.Tissue SpV (%)	84 vs. 88		>.9999[e]
DIV-MAC vs. CONV-UTM		**85 vs. 94**		.0205[e]
CONV-MAC vs. CONV-UTM		88 vs. 94		.2516[e]
DIV-MAC vs. CONV-MAC	Conn.Tissue DA	0.55 vs. 0.51		.8607[d]
DIV-MAC vs. CONV-UTM		0.55 vs. 0.55		.9992[d]
CONV-MAC vs. CONV-UTM		0.51 vs. 0.55		.8507[d]
DIV-MAC vs. CONV-MAC	Conn.Tissue ConnD ($\times 10^{-3}$ px^{-3})	1.8 vs. 2.1		.5444[d]
DIV-MAC vs. CONV-UTM		**1.8 vs. 2.5**		.0430[d]
CONV-MAC vs. CONV-UTM		2.1 vs. 2.5		.3141[d]

Note: Statistically significant values ($p < .05$) in bold.
[a]Mean ± SE, median values.
[b]Ordinary one-way ANOVA test.
[c]Kruskal–Wallis test.
[d]Tukey's multiple comparisons test.
[e]Dunn's multiple comparisons test.

Moreover, to compare amount and 3D distribution of collagen in the three experimental groups, the full 3D morphometric analysis was performed on the complete set of samples. Several stack-sequences of sub-volumes (each with a final volume of 540 × 270 × 270 μm^3, with the longest side of the prism as close as possible to the mucosa/abutment interface and mapping the complete biopsies in the longitudinal direction) have been considered and morphometrically investigated. Radially, that is, in planes transverse to the direction of the implant axis, the prisms had a maximum distance from the interface of about 300–400 μm. Vertically, that is, parallel to the direction of the axis of the implant, they were stacked one after the other until reaching, for each sample, the maximum height of the connective tissue in contact with the implant. Representative subvolumes (prisms) of the DIV-MAC, CONV-MAC, and CONV-UTM groups are reported in **Figure 23a–c**. The full 3D collagen morphometric quantification, including the shape and 3D complexity

analysis, is reported in **Figure 23d-f** and **Table 2**. For each sample, we considered subvolumes in which the amount of collagen was maximally expressed, that is, with the highest SpV values.

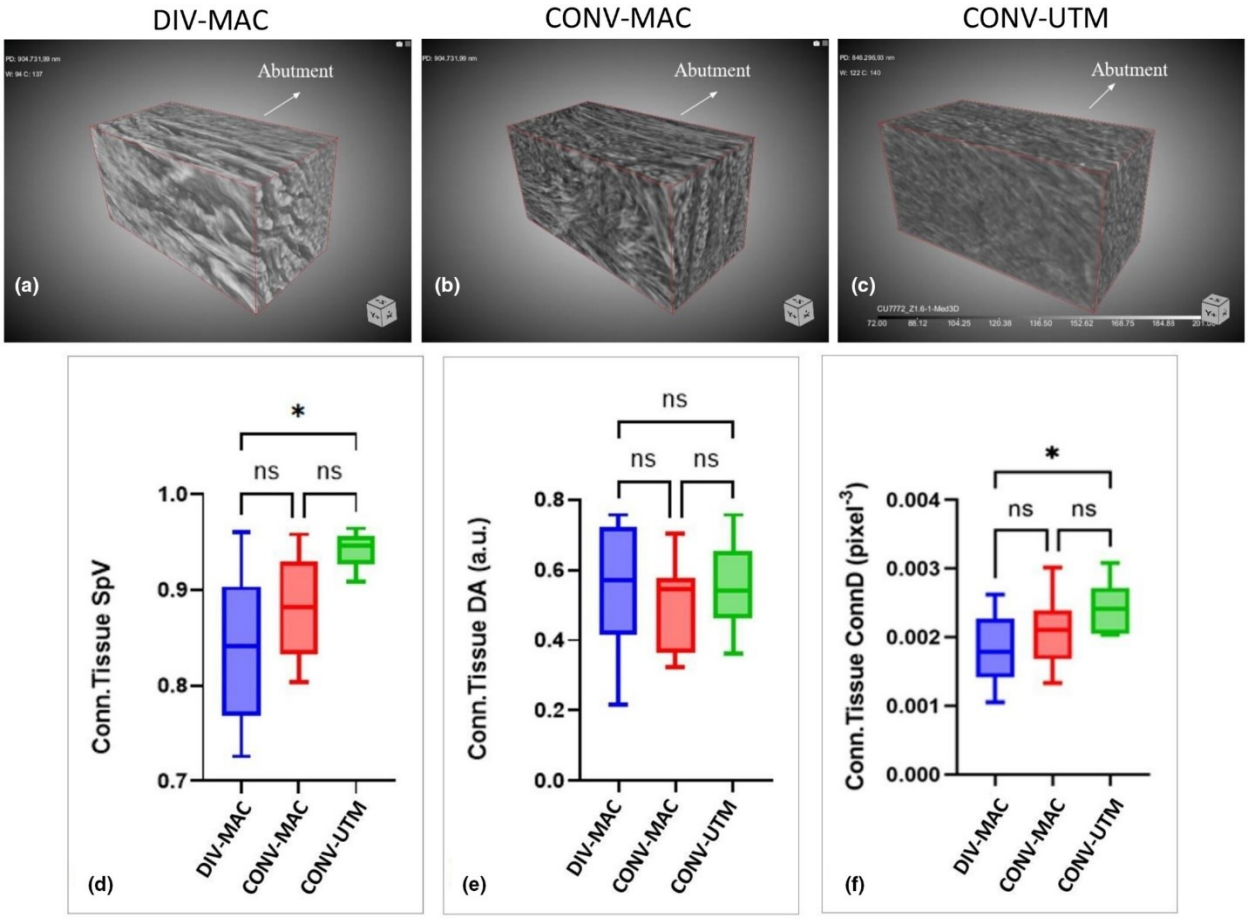

Figure 23 - *(a–c) Synchrotron 3D reconstructions of representative subvolumes (each with a fixed dimension of 540 × 270 × 270 μm³ and with the longest side of the prism as close as possible to the interface with the abutment) of the (a) DIV-MAC, (b) CONV-MAC, and (c) CONV-UTM groups: The decreased contrast between collagen fibers and interstitial spaces in the CONV-UTM group is an indication of an increased amount and interlacing of the collagen bundles. (d–f) Synchrotron imaging Data Analysis. Box-and-whisker diagram of the distribution of PhC-μCT morphometric parameters: (d) connective tissue specific volume (Conn.Tissue SpV – %), (e) connective tissue anisotropy degree index (Conn.Tissue DA), and (f) connective tissue connectivity density (Conn.Tissue ConnD – pixel^{-3}). Statistical comparison among the three experimental groups (i.e., DIV-MAC, CONV-MAC, CONV-UTM). Upper and lower ends of boxes represent 75th and 25th percentiles. The median value is showed with a solid line. *p < .05 (*[84], *CC-BY 4.0).*

As regards the Conn.Tissue SpV parameter, the Kruskal–Wallis test, applied because equivariance was not verified, showed differences among the three experimental groups (**Table 2**). In particular, Dunn's multiple comparisons test indicated differences between the DIV group and CONV-UTM, with a significantly higher value for the last group.

As regards the Conn. Tissue DA parameter, the ordinary one-way ANOVA test, applied because normality and homogeneity of variances were verified, showed no differences among the three experimental groups (**Table 2**).

As regards the Conn.Tissue ConnD parameter, the ordinary one-way ANOVA test, applied because normality and homogeneity of variances were verified, showed no differences among the three experimental groups (**Table 2**). However, Tukey's multiple comparisons test indicated differences between the DIV-MAC and CONV-UTM groups ($p = .0430$), with a significantly higher value for the last group.

From the qualitative analysis emerged a clear positive impact of the convergent geometry respect to the divergent one: a significantly higher connective tissue was found around both convergent groups. Moreover, the micro-grooved surface outperformed the machined one, in terms of intertwined collagen bundle density. A subtle implication of this result is that collagen amount and collagen fibers distribution can be considered and evaluated as independent quality factors for the healing tissue.

Interesting consideration can also be carried on the biomechanics underlying these morphological responses. Structural forces exerted during the healing process heavily relies on the geometrical conditions met in the surroundings, which influence the directionality and the morphological complexity of the resulting connective tissue. In turn, being aware of the physical responses can provide valuable insights into tissue stability.

These results are particularly valuable as they have a direct impact in implantology clinical practice: the influence of abutment macro-and micro-geometries on peri-implant tissue has been a frequent topic of research over the last decades. Its comprehension can reduce the failure rate of oral implant surgery.

3.2.3 Oral Pathology: tongue squamous cell carcinoma

In this last research, as the previous ones, the study was the result of a multidisciplinary collaboration between some research groups: namely, physicists and oral pathologists of the Department of Odontostomatologic and Specialized Clinical Sciences, chemists of the Department of Life and Environmental Sciences of the Marche Polytechnic University, a patologist of the Department of Biomedical Sciences and Public Health (Marche Polytechnic University), the Dentistry Clinic of the National Institute of Health and Science of Aging, IRCCS INRCA and a PhD student of the Department of Neuroscience, Imaging and Clinical Sciences of the University G. d'Annunzio of Chieti-Pescara. The full manuscript is not yet published but is under review at the journal iScience.

- *Background of the study*:

Oral squamous cell carcinoma (OSCC) is the most prevalent malignancy affecting the head and neck region, with an annual global incidence of over 370,000 cases, constituting more than 90% of all oral cavity cancers. Among oral cancers, OSCC frequently originates from various oral regions, with the tongue (OTSCC) being the most commonly affected, accounting for up to 40% of all cases [86].

While the significance of the tumor microenvironment (TME) in oral cancer has been acknowledged for over a decade, its pathological assessment and staging primarily relies on the morphological characteristics of parenchyma, the tumor itself. However, the stroma, a key component of the TME, plays a crucial role in tumor progression, invasion, metastasis, and resistance to therapy [87]. Comprising non-malignant cells such as cancer-associated fibroblasts (CAF), specialized mesenchymal cells, immune cells, endothelial cells, pericytes, and the extracellular matrix (ECM), the tumor stroma actively influences the development of an aberrant tumor phenotype. Notably, alterations in the stroma are observed early in carcinogenesis, preceding the manifestation of recognizable epithelial dysplasia [88].

Studies have shown that in OTSCC, tumors with a higher stromal component, exhibit worse disease-specific survival (DSS) and overall survival (OS) compared to those with a lower stromal content [87], [89].

Therefore, this study aims to investigate the morphology of the tumor stroma in OTSCC and analyze the ultrastructure of collagen tissue and the configuration of its fibers.

The retrospective study included 36 selected patients with histological diagnosis of OTSCC. Nr. 36 biopsies, stored in the Oral Pathology Institutional Archive, corresponding to as many patients, were sectioned by a 13-gauge bone-marrow transplant needle (HS Hospital Service SpA, Aprilia, Italy) until cylindrical samples embedded in paraffin were obtained. Two cylindrical sections (diameter about 2 mm) were cut from each block from the most invasive area with the highest percentage of desmoplastic stroma, where tumour cell nests were present at all borders of the selected image field.

- *Synchrotron Radiation Phase Contrast High Resolution Tomography application:*

The PhC-microCT scanning was performed at the SYRMEP beamline of the ELETTRA Synchrotron Facility (Basovizza, Trieste, Italy).

The scans were performed using a pink X-ray beam filtered by a silicon plate with thickness = 0.5 mm; an energy peak of 17 keV; an exposure time of 0.2 s per projection with angular step of 0.1°. The sample-detector distance was 100 mm, resulting in an isotropic voxels size of 890 nm.

The tomographic reconstructions were performed using the open-source software SYRMEP Tomo Project (STP) [73], through the Paganin's method for the phase recovery algorithm [52]. The δ/β ratio was set to 100.

For each sample, a volume of 2048 × 2048 × 2048 pixel^3 was acquired and reconstructed; it corresponded to a volume of about 6 mm3. Within each reconstructed sample, volumes of interest (VOIs) were extrapolated in the intratumoral stroma (i.e. in the stroma scattered between the neoplastic cords and/or islets), in the peritumoral stroma (i.e. along the infiltrative front near the neoplastic epithelial cells and/or islets infiltrating the surrounding stroma) and in the extratumoral stroma, following expert pathologists indications and using 3D visualization and orthographic projection in Dragonfly software (v. 2024.1, ORS, Montréal, Quebec) (**Figure 24**) and pre-processed by the Frangi3D filter.

The complete morphometric analysis was performed using FIJI (ImageJ distribution Software) [74] to characterize the following morphological indices: the collagen specific volume (Vol.%), measuring the ratio between the collagen voxels volume and the total volume of the investigated VOI; the mean collagen bundle Thickness (Th; μm) and the mean collagen bundle Spacing (Sp; μm), measuring the mean distance between two collagen bundles. The shape and the 3D-complexity indices were also calculated: the Anisotropy Degree (DA), varying between 0 (perfect isotopically distribution of collagen bundles) and 1 (collagen bundles oriented in the same direction); the Connectivity Density (Conn.D; μm^{-3}), showing higher values for better-connected collagen bundles and lower values for poorly connected ones; and the 3D-Fractal Dimension (Fr.Dim), ranging from 2 to 3 and indicating at which extend an irregular structure fills the space at different scales. The box-counting algorithm, with the following starting setup was used: box initial size [px]: 48; smallest box size [px]: 6; box scale factor: 1.2; grid translation: 0.

The statistical analysis was performed using GraphPad Prism version 8.00 (GraphPad Software) and SPSS statistical software version 25.0 (IBM Corporation). One-way analysis of variance (ANOVA) and Tukey's multiple comparisons test evaluated the differences among examined groups.

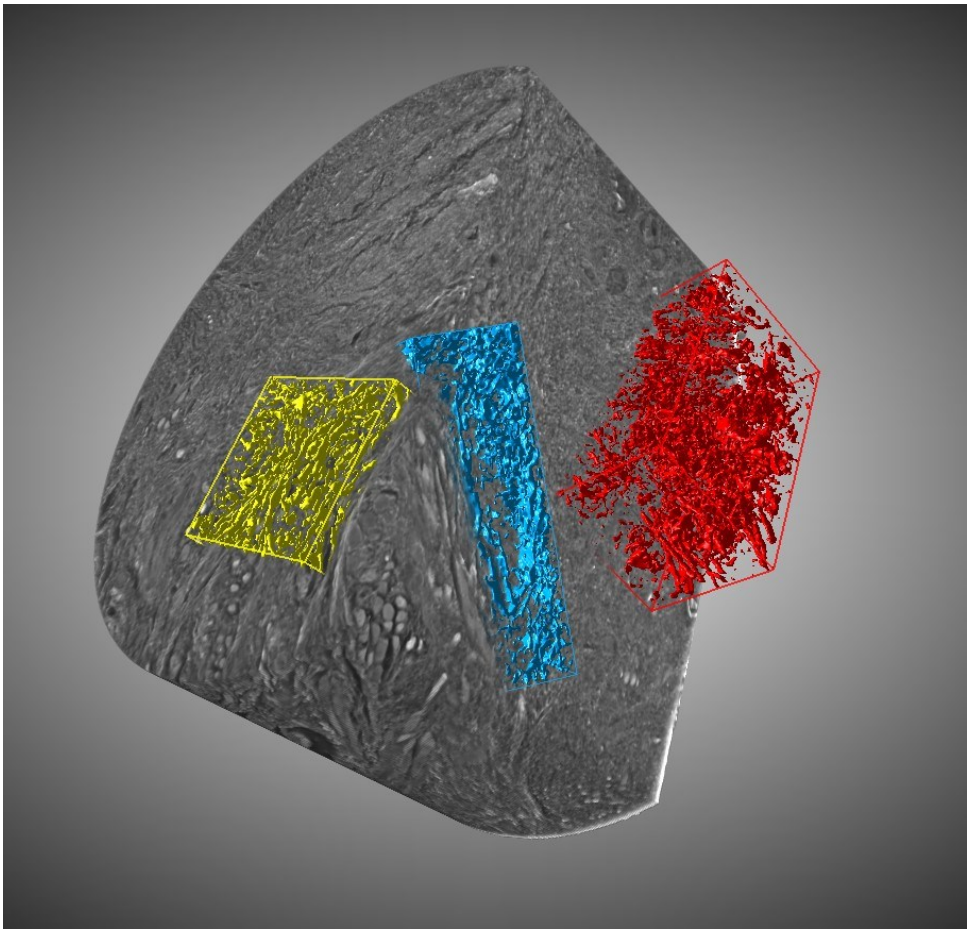

Figure 24 – *A 3D visualization of the whole acquired volume and, highlighted in different colors, box situated within the three different stromal compositions: extratumoral (yellow), peritumoral (blue), intratumoral (red).*

- *Results*:

The 3D synchrotron imaging showed the presence of a dense and well-organized extratumoral stroma; conversely, the intratumoral and peritumoral regions seemed characterized by loosely packed and randomly arranged collagen bundles, resulting in an oedematous stroma, regardless the pathological stage.

The statistical analysis revealed the presence of wide variability for all morphometric parameters. Repeated measures analysis of variance and Tukey's multiple comparisons test evaluated the differences among the tumoral regions. The full PhC-microCT data analysis is reported in **Figure 25**, by Box-and-whisker diagrams.

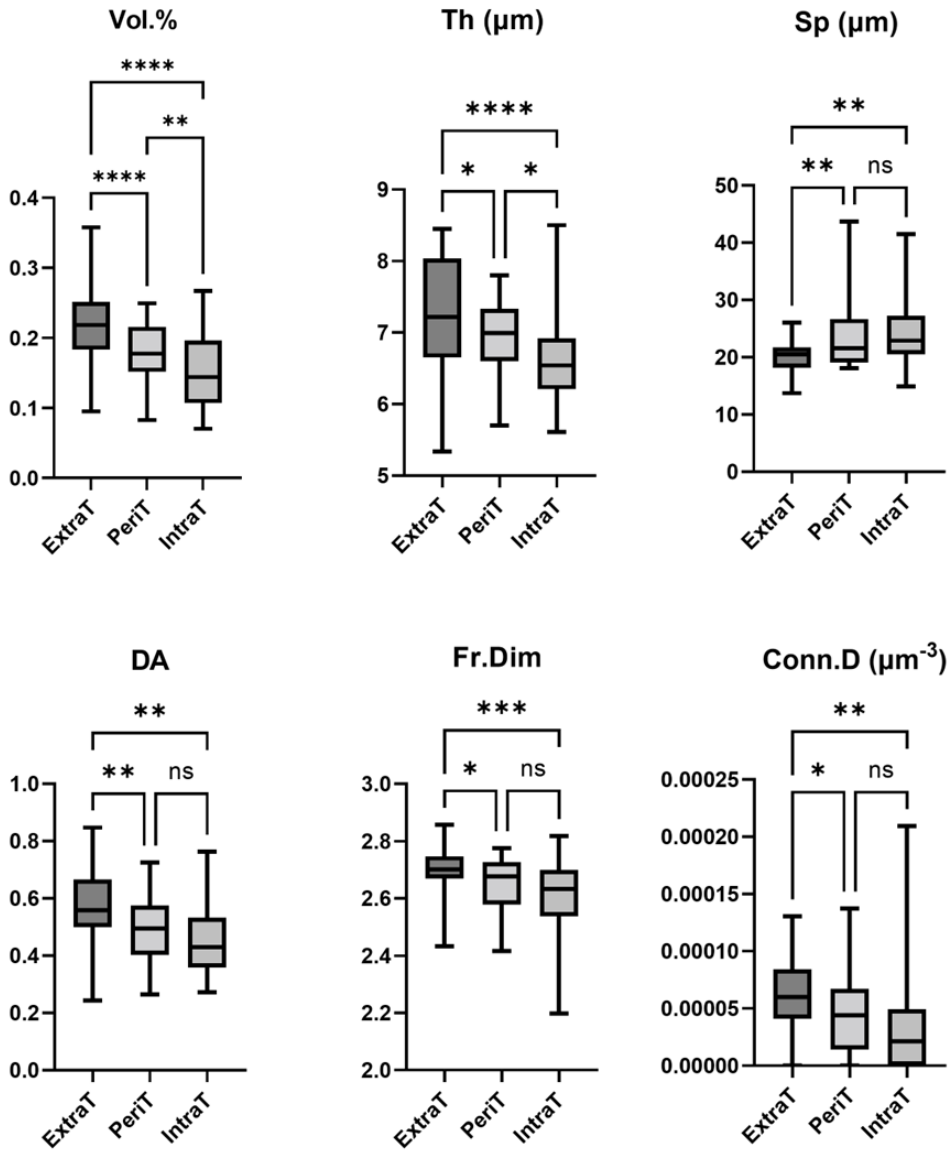

Figure 25 - *PhC-microCT data analysis. Collagen morphometric parameters calculated in the extratumoral (ExtraT), peritumoral (PeriT), and intratumoral (IntraT) stroma of OTSCC samples. Box-and-whisker diagrams of the distribution of PhC-microCT morphometric parameters: connective tissue specific volume (Vol.% - [0÷1]), collagen bundles mean thickness (Th - µm), collagen bundles mean spacing (Sp - µm), connective tissue anisotropy degree index (DA- [0÷1]), connective tissue 3D fractal dimension (Fr.Dim - [2÷3]) and connective tissue connectivity density (Conn.D – μm^{-3}). Upper and lower ends of boxes represent 75th and 25th percentiles. Max and min valued are reported. The median value is showed with a solid line. *P < .05; **P < .01; ***P < .001; ****P < .0001. Number of biopsies investigated: 35, one for each patient.*

The volume percentage significantly increased from intratumoral to peritumoral and extratumoral stroma. Similarly, the extratumoral bundles were significantly thicker, both respect to peritumoral and intratumoral ones. Limitedly to these two parameters, statistically significant differences were also detected comparing peritumoral and intratumoral stroma. The spacing between bundles significantly decreased from extratumoral to peritumoral and intratumoral stroma. Anisotropy degree, fractal dimension, and connectivity density were significantly higher in the extratumoral stroma compared to peritumoral and intratumoral ones. Interestingly, no significant differences ($P > 0.05$) were found between peritumoral and intratumoral stroma for spacing between bundles, anisotropy degree, fractal dimension and connectivity density.

Moreover, one-way ANOVA and Tukey's multiple comparison test did not reveal significant differences of the morphometric indices among the OTSCCs pathological stages in the peritumoral stroma (data not shown).

These morphometrical data revealed the presence of wide variability for all the parameters, also in the extratumoral regions: this could be related to the structural heterogeneity of the stroma between the different collected areas among the patients, confirming that the tongue is an anatomical site extremely heterogeneous from a microarchitectural point of view. For this reason, statistical analysis was performed through repeated measures analysis of variance, comparing each extratumoral area with the corresponding peritumoral and intratumoral ones (**Figure 25**). We observed and quantified the presence of a reduced amount of collagen bundles, thinner and more spaced near to the tumor parenchyma: this result could suggest the presence of an immature collagen (intratumoral area), which is usually observed in infiltrative tumors, while a greater amount of thicker and closer collagen bundles should be attributable to a mature and physiological collagen (extratumoral area). In this direction, other authors confirmed the prevalence of thin collagen bundles in metastatic and advanced-stage tumors [90], [91]. Synchrotron imaging data also demonstrated that the intratumoral area has a greater isotropy, a smaller fractal dimension, and a very reduced connectivity with respect to the extratumoral areas: this information, read together in the light of a biomechanical rationale, outline evidence of compromised mechanical strength and tissue tension, and could explained the extreme dysfunctionality of the tumoral and

peritumoral stroma. Thus, in the peritumoral and intratumoral stroma, the collagen alterations could promote the clustering of the neoplastic cells in small nests, supporting the epithelial-to-mesenchymal transition (EMT). Synchrotron PhC-microCT results are corroborated by literature data; indeed, it has been demonstrated that collagen bundles arrangement undergoes to a progressive disorganisation from clinically healthy mucosa to advanced carcinomas [92], [93].

3.3 Discussion of the results

Acquiring and analyzing data from diverse samples has been challenging due to the lack of real guidelines in this field. In fact, as described in the first chapter, with the different methodologies for imaging collagen structures, none of them represented the declared gold standard for characterization. Arguably, the relatively new interest in the role and behavior of this tissue is partly responsible for the various methods used in scientific research to examine it.

Citing from Nejim et al. [22], referring to SHG images "...The choice of the method still depends on the images that need to be processed, their quality, and the error tolerance rate. A proper quantitative analysis of collagen fibers needs a combination of some of the techniques presented previously. On the other hand, the quantitative analysis of collagen fibers in 3D is still not widely developed because of the limitations of the acquisition technique when going deep into the tissue and the poor imaging resolution in the third dimension. Further studies need to be oriented toward this issue especially because it is important to quantify the fiber network in the 3D space."

From our perspective, the ability of PhC-μCT to provide a three-dimensional representation of collagen organization and architecture represents a significant advantage. This is particularly true because it allows the sample to be observed from various planes across the reconstructed stack, effectively incorporating also two-dimensional information. Furthermore, the acquisition of the tissue as a whole allowed us to investigate how collagen interacts with the parenchyma in which it is immersed. This aspect is crucial when evaluating what is relevant for research within a multidisciplinary team, including clinicians.

4 Future developments

Exploring the potential of PhC-microCT for soft tissues holds significant promise for future development, conceptually simply divided into two macro-categories: functional applications to clinical context and technical advancement.

By leveraging the enhanced knowledge acquired through this powerful imaging modality, we can envisage various functional applications for the human body. Specifically referring to collagen structures, as discussed in the Introduction chapter, they play a crucial role for the tissue tensioning and contraction. However, collagens' architecture and mechanics govern not only the tissue's overall responses, but also the functions of the cells that reside within it. Collagen fibers supply cells with topographical, biochemical, and mechanical signals that regulate cell proliferation, differentiation, migration, and death [4].

To effectively address these responses, it is critical to comprehend the intricate signaling pathways contributing to their formation. While early investigations predominantly centered on biochemical mechanisms, recent studies have underscored the significant influence of mechanical forces in regulating these pathways [2], [94], [95]. This recognition emphasizes the importance of considering both biochemical and mechanical factors in developing strategies to predict and prevent negative outcomes. Understanding how external forces impact collagen organization and therefore its role in physiologic and pathologic conditions, will assist physicians in controlling tissue alterations [96]. This may apply to wound healing and scarring for physiologic studies, as presented in paragraph 3.2.2, or fibrosis and cancer formation for pathologic research, paragraphs 3.1, 3.2.1 and 3.2.3.

On the other hand, considering technical advancement, it is surely worth of attention the development of new artificial intelligence (AI) tools, capable of automating and making more efficient the various stages that lead to a scientific relevant result. This may include the already mentioned phase retrieval algorithms, as well as reconstruction algorithms. Both these steps contribute to the improvement of the final image quality and to artifacts reduction. However, at the present time, even more could still be achieved when it comes

to image elaboration. This may refer to image segmentation, features selection and extraction. An example, which relates to the results presented in section 3.2.2, is the application of Convolutional Neural Networks (CNN) to discriminate the orientation of collagen fibers surrounding the dental implant abutment and segment differently oriented bundles based on their directionality (**Figure 26**) [97]. This example also proves the AI tools intrinsic nature of being extremely result oriented, and therefore specific for each application, producing increasingly accurate and reliable results. For instance, a big effort was put, and interesting results have been achieved, in classification of lung disease, pushed by recent COVID-19 pandemic [98], [99]. Still a lot could be done in a lot of different contexts. To mention two of great interest and relevance, early diagnosis and prevention, especially in oncology [100].

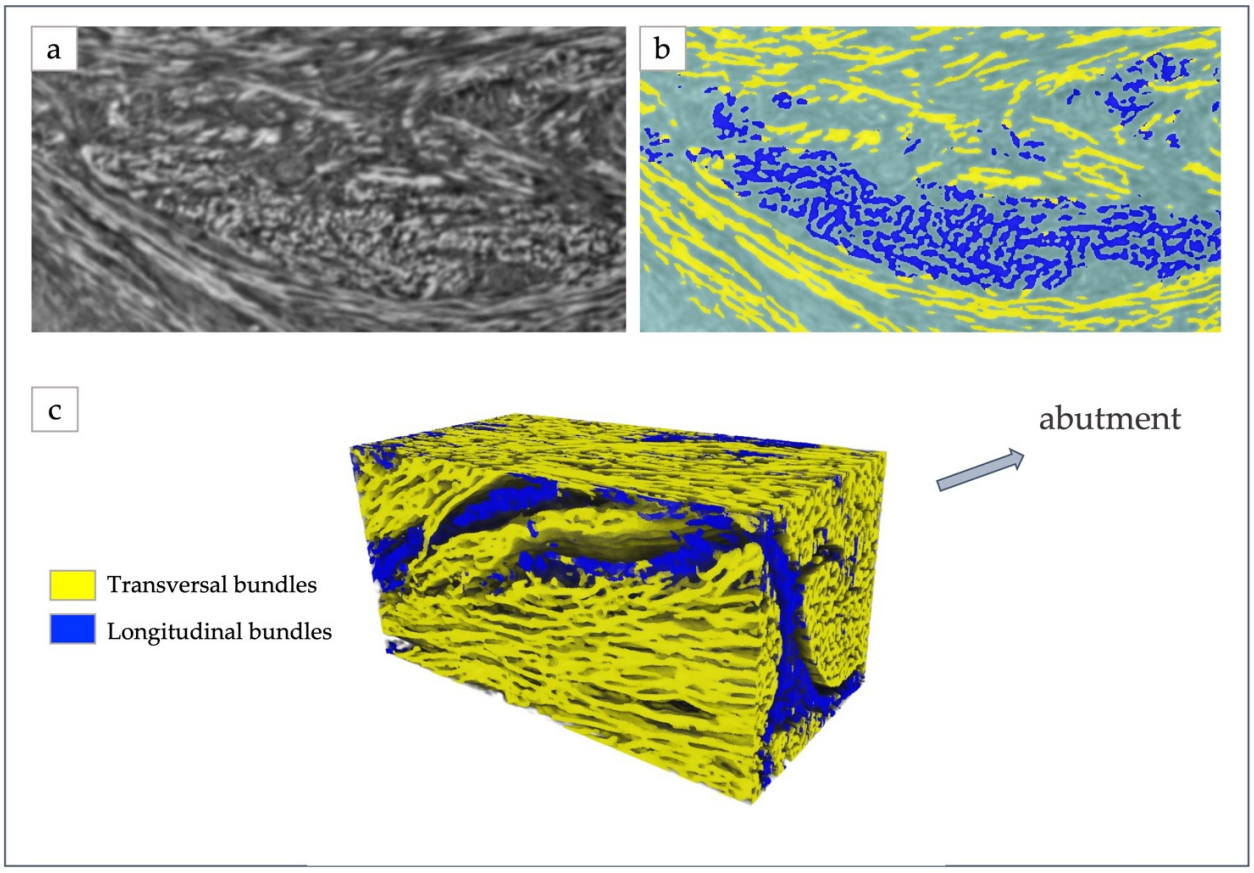

Figure 26 – *(a) Raw slice of a subvolume of* sample1*, as achieved after phase-retrieval reconstruction; (b) semantic segmentation of the same slice with deep learning: transversal bundles (yellow), longitudinal bundles (blue) and background (teal) were detected. (c) Application of artificial intelligence to a subvolume*

of sample2 *and automatic segmentation of collagen bundles (blue: longitudinal; yellow: transversal) (*[97], *CC-BY 4.0).*

Overall, it could be said that in recent years we have witnessed a revolution due to the possibility of using color images as input data for deep learning models. Imagining a turn of events in the near future, approaches that rely primarily on single types of data may miss important predictive insights arising from the interaction of interconnected biological systems. Consequently, there is a push to combine multimodal data, so-called multi-Omics data inputs (including radiomics, genomics, transcriptomics, metabolomics and clinical aspects), in order to fully characterize the landscape and improve the accuracy of diagnosis. Therefore, PhC-tomographic images will become part of a whole, which will be able - hopefully - to fully understand the problem we are facing. This direction is, in turn, a natural consequence of what has been described in this thesis as the effort to achieve a multidisciplinary approach.

Another point worth discussing is the expansion of opportunities to access high-resolution images obtained with phase contrast, without having to interface with large research facilities such as synchrotrons. Towards wider accessibility and use of this technique in the clinical field, the conversion from the synchrotron to laboratory sources is an important objective that involves numerous disciplinary fields aimed at continuous development of the method and of the supporting hardware/software technology.

Laboratory-based phase-contrast tomography has already been implemented at different X-Ray sources: transmission microfocus sealed tubes [101], liquid metal-jet anodes [102], as well as microfocus rotating-anode sources [103]. The detection technology has been equally diverse: in this direction, nanotubes offer yet another opportunity to implement phase-contrast tomography with possible advantages (**Figure 27**), in particular, in view of increased spatial coherence length [104].

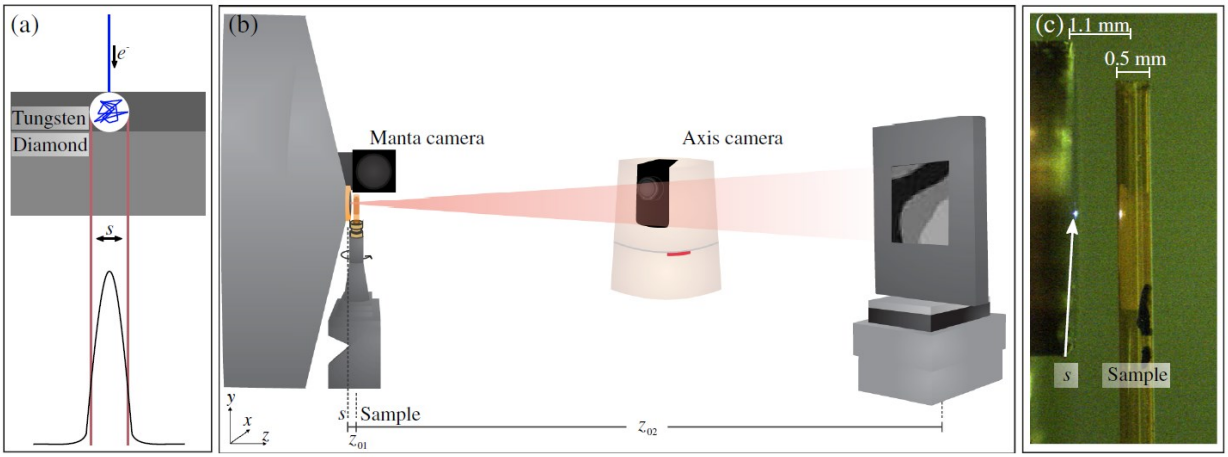

Figure 27 - *Illustration of the nanotube setup: (a) schematic of the transmission target x-ray source; (b) recording geometry: the cone-shaped front end of the nanotube allows for small distances z01 between source s and the sample. The detector is aligned at z02 from the source. The axis camera allows for visual inspection of the setup in general, while the Manta camera gives a microscopic control of the tight z01 environment; see exemplary view in (c).* ([104], *CC-BY 4.0)*

The high number of groups testing different setups to achieve a good ratio between sensitivity and setup technological constrains [105], is a proof of the growing interest in a robust way to obtain good contrast for soft tissues – like collagen-based ones – with laboratory instrumentation, with the ultimate goal of introducing this technique into clinical practice within hospitals.

Bibliography

[1] P. Fratzl, "Collagen: Structure and Mechanics, an Introduction BT - Collagen: Structure and Mechanics," P. Fratzl, Ed. Boston, MA: Springer US, 2008, pp. 1–13.

[2] B. Kuehlmann, C. A. Bonham, I. Zucal, L. Prantl, and G. C. Gurtner, "Mechanotransduction in wound healing and fibrosis," *J. Clin. Med.*, vol. 9, no. 5, pp. 1–19, 2020, doi: 10.3390/jcm9051423.

[3] M. J. Buehler and Y. C. Yung, "Deformation and failure of protein materials in physiologically extreme conditions and disease," *Nat. Mater.*, vol. 8, no. 3, pp. 175–188, 2009, doi: 10.1038/nmat2387.

[4] F. B. Kai, H. Laklai, and V. M. Weaver, "Force Matters: Biomechanical Regulation of Cell Invasion and Migration in Disease," *Trends Cell Biol.*, vol. 26, no. 7, pp. 486–497, 2016, doi: 10.1016/j.tcb.2016.03.007.

[5] K. Song, Z. Yu, X. Zu, G. Li, Z. Hu, and Y. Xue, "Collagen Remodeling along Cancer Progression Providing a Novel Opportunity for Cancer Diagnosis and Treatment," *Int. J. Mol. Sci.*, vol. 23, no. 18, 2022, doi: 10.3390/ijms231810509.

[6] S. Xu *et al.*, "The role of collagen in cancer: From bench to bedside," *J. Transl. Med.*, vol. 17, no. 1, pp. 1–22, 2019, doi: 10.1186/s12967-019-2058-1.

[7] S. W. Chang and M. J. Buehler, "Molecular biomechanics of collagen molecules," *Mater. Today*, vol. 17, no. 2, pp. 70–76, 2014, doi: 10.1016/j.mattod.2014.01.019.

[8] H. G. Davis, *Conservative surgery, as exhibited in remedying some of the mechanical causes that operate injuriously both in health and disease.* New York: D. Appleton & Company, 1867.

[9] K. Lundon, "The Effects of Mechanical Load on Soft Connective Tissues," in *Functional Soft-Tissue Examination and Treatment by Manual Methods*, Boston, MA: Jones and Bartlett, Inc., 2007.

[10] L. Salvatore, N. Gallo, M. L. Natali, A. Terzi, A. Sannino, and M. Madaghiele, "Mimicking the Hierarchical Organization of Natural Collagen: Toward the Development of Ideal Scaffolding Material for Tissue Regeneration," *Front. Bioeng. Biotechnol.*, vol. 9, no. April, 2021, doi: 10.3389/fbioe.2021.644595.

[11] L. PAULING and R. B. COREY, "The structure of fibrous proteins of the collagen-gelatin group.," *Proc. Natl. Acad. Sci. U. S. A.*, vol. 37, no. 5, pp. 272–281, May 1951, doi: 10.1073/pnas.37.5.272.

[12] D. A. D. Parry, G. R. G. Barnes, and A. S. Craig, "A comparison of the size distribution of collagen fibrils in connective tissues as a function of age and a possible relation between fibril size distribution and mechanical properties," *Proc. R. Soc. London - Biol. Sci.*, vol. 203, no. 1152, pp. 305–321, 1978, doi: 10.1098/rspb.1978.0107.

[13] D. A. D. Parry, "The molecular fibrillar structure of collagen and its relationship to the mechanical properties of connective tissue," *Biophys. Chem.*, vol. 29, no. 1, pp. 195–209, 1988, doi: https://doi.org/10.1016/0301-4622(88)87039-X.

[14] M. J. Buehler, "Nanomechanics of collagen fibrils under varying cross-link densities: Atomistic and continuum studies," *J. Mech. Behav. Biomed. Mater.*, vol. 1, no. 1, pp. 59–67, 2008, doi: 10.1016/j.jmbbm.2007.04.001.

[15] A. Gautieri, S. Vesentini, A. Redaelli, and M. J. Buehler, "Hierarchical structure and nanomechanics of collagen microfibrils from the atomistic scale up," *Nano Lett.*, vol. 11, no. 2, pp. 757–766, 2011, doi: 10.1021/nl103943u.

[16] N. I. Dibal, S. H. Garba, and T. W. Jacks, "Histological stains and their application in teaching and research," *Asian J. Heal. Sci.*, 2022, [Online]. Available: https://api.semanticscholar.org/CorpusID:254558142.

[17] F. Deng, J. Miller, and T. Swanson, "Histology revolution: From inefficient, two-dimensional, and low- resolution techniques to high-throughput, three-dimensional and high-resolution techniques," *Egypt. J. Histol.*, vol. 43, no. 2, pp. 373–379, 2020, doi: 10.21608/ejh.2019.16977.1168.

[18] A. Keikhosravi *et al.*, "Real-time polarization microscopy of fibrillar collagen in histopathology," *Sci. Rep.*, vol. 11, no. 1, pp. 1–11, 2021, doi: 10.1038/s41598-021-98600-w.

[19] G. Balezo, C. Bertram, C. Tilmant, S. Petit, S. Hadj, and R. Fick, "Enabling Collagen Quantification on HE-Stained Slides through Stain Deconvolution and Restained HE-HES," in *2023 IEEE 20th International Symposium on Biomedical Imaging (ISBI)*, 2023, pp. 1–5, doi: 10.1109/ISBI53787.2023.10230681.

[20] T. H. I. Tram, A. N. H. Pham, H. Kim, Y. Lee, and S. Park, "Universal Convolutional Neural Network for Histology-Independent Analysis of Collagen Fiber Organization in Scar Tissue," *IEEE Access*, vol. 10, pp. 34379–34392, 2022, doi: 10.1109/ACCESS.2022.3162272.

[21] A. D. I. B. K. Eikhosravi *et al.*, "Quantification of collagen organization in histopathology samples using liquid crystal based polarization microscopy," *Biomed. Opt. Express*, vol. 8, no. 9, pp. 4243–4256, 2017, doi: https://doi.org/10.1364/BOE.8.004243.

[22] Z. Nejim, L. Navarro, C. Morin, and P. Badel, "Quantitative analysis of second harmonic generated images of collagen fibers : a review," *Res. Biomed. Eng.*, pp. 273–295, 2023, doi: 10.1007/s42600-022-00250-y.

[23] A. Aghigh, S. Bancelin, M. Rivard, M. Pinsard, H. Ibrahim, and F. Légaré, "Second harmonic generation microscopy: a powerful tool for bio-imaging," *Biophys. Rev.*, vol. 15, no. 1, pp. 43–70, 2023, doi: 10.1007/s12551-022-01041-6.

[24] M. Han, G. Giese, and J. F. Bille, "Second harmonic generation imaging of collagen fibrils in cornea and sclera," *Opt. Express*, vol. 13, no. 15, p. 5791, 2005, doi: 10.1364/opex.13.005791.

[25] M. Sendín-Martín *et al.*, "Quantitative collagen analysis using second harmonic generation images for the detection of basal cell carcinoma with ex vivo multiphoton microscopy," *Exp. Dermatol.*, vol. 32, no. 4, pp. 392–402, 2023, doi: 10.1111/exd.14713.

[26] Y. Birman, S. Khorsand, E. Tu, R. B. Mortensen, and M. T. Butko, "Second-harmonic generation-based methods to detect and characterize ligand-induced RNA conformational changes," *Methods*, vol. 167, no. May 2019, pp. 92–104, 2019, doi: 10.1016/j.ymeth.2019.05.012.

[27] F. Benattia, Z. Arrar, and F. dergal, "Methods and Applications of Raman Spectroscopy : A Powerful Technique in Modern Research, Diagnosis, and Food Quality Control," *Curr. Nutr. Food Sci.*, vol. 20, pp. 41–61, 2023, doi: 10.2174/1573401319666230503150005.

[28] Á. Fernández-galiana, O. Bibikova, S. V. Pedersen, and M. M. Stevens, "Fundamentals and Applications of Raman-Based Techniques for the Design and Development of Active Biomedical Materials," *Adv. Mater.*, vol. 2210807, pp. 1–47, 2023, doi: 10.1002/adma.202210807.

[29] S. Kiss, S. Chintapatla, and R. Kroger, "DD-04 INVESTIGATING COLLAGEN IN INCISIONAL HERNIA MIDLINE SCARS USING RAMAN SPECTROSCOPY," *Br. J. Surg.*, vol. 109, 2022, doi: 10.1093/bjs/znac308.008.

[30] L. Becker *et al.*, "Raman microspectroscopy identifies fibrotic tissues in collagen-related disorders via deconvoluted collagen type I spectra," *Acta Biomater.*, vol. 162, pp. 278–291, 2023, doi: 10.1016/j.actbio.2023.03.016.

[31] H. Ye, U. Kruger, T. Wang, S. Shi, and J. Nor, "Burn-related Collagen Conformational Changes in ex vivo Porcine Skin using Raman Spectroscopy," *Sci. Rep.*, pp. 1–9, 2019, doi: 10.1038/s41598-019-55012-1.

[32] M. S. Bergholt, A. Serio, M. B. Albro, and M. B. Albro, "Raman Spectroscopy : Guiding Light for the Extracellular Matrix," *Front. Bioeng. Biotechnol.*, vol. 7, no. November, pp. 1–16, 2019, doi: 10.3389/fbioe.2019.00303.

[33] E. Shehata, E. Nippolainen, R. Shaikh, A. Petteri, and R. Juha, "Raman Spectroscopy and Machine Learning Enables Estimation of Articular Cartilage Structural , Compositional , and Functional Properties," *Ann. Biomed. Eng.*, vol. 51, no. 10, pp. 2301–2312, 2023, doi: 10.1007/s10439-023-03271-5.

[34] L.-A. DiCecco, R. Gao, J. L. Gray, D. F. Kelly, E. D. Sone, and K. Grandfield, "Liquid Transmission Electron Microscopy for Probing Collagen Biomineralization.," *Nano Lett.*, vol. 23, no. 21, pp. 9760–9768, Nov. 2023, doi: 10.1021/acs.nanolett.3c02344.

[35] B. V Rego, D. Weiss, and J. D. Humphrey, "A fast, robust method for quantitative assessment of collagen fibril architecture from transmission electron micrographs.," *bioRxiv : the preprint server for biology*. United States, Feb. 2023, doi: 10.1101/2023.02.06.527383.

[36] T. Starborg *et al.*, "Using transmission electron microscopy and 3View to determine collagen fibril size and three-dimensional organization," *Nat Protoc.*, vol. 8, no. 7, pp. 1433–1448, 2017, doi: 10.1038/nprot.2013.086.Using.

[37] J. Ha, "Physical Principles and Equipment of Intravascular Optical Coherence Tomography," in *Coronary Imaging and Physiology*, M.-K. Hong, Ed. Singapore: Springer Singapore, 2018, pp. 97–106.

[38] K. M. Lee, "Principles of OCT Imaging BT - OCT Imaging in Glaucoma: A guide for practitioners," K. H. Park and T.-W. Kim, Eds. Singapore: Springer Singapore, 2021, pp. 1–12.

[39] B. E. Bouma *et al.*, "Optical coherence tomography," *Nat Rev Methods Prim.*, vol. 2, no. 79, 2022, doi: 10.1038/s43586-022-00162-2.

[40] Y. Alexandrovskaya *et al.*, "Optical Coherence Elastography as a Tool for Studying Deformations in Biomaterials : Spatially-Resolved Osmotic Strain Dynamics in Cartilaginous Samples," *Materials (Basel).*, vol. 15(3), 904, 2022, doi: https://doi.org/10.3390/ma15030904.

[41] P. Tang *et al.*, "Polarization sensitive optical coherence tomography with single input for imaging depth-resolved collagen organizations," *Light Sci. Appl.*, vol. 10:237, 2021, doi: 10.1038/s41377-021-00679-3.

[42] T. M. Cannon, N. U. Patarroyo, M. Villiger, and B. E. Bouma, "Measuring collagen injury depth for burn severity determination using polarization sensitive optical coherence tomography," *Sci. Rep.*, no. 0123456789, pp. 1–11, 2022, doi: 10.1038/s41598-022-14326-3.

[43] L. Yang, R. R. Iyer, J. E. Sorrells, E. J. Chaney, and S. A. Boppart, "Combining linear and nonlinear polarization-sensitive imaging modalities for enhanced characterizations of collagen," in *Biophotonics Congress: Biomedical Optics 2022 (Translational, Microscopy, OCT, OTS, BRAIN)*, 2022, p. MW3A.1, doi: 10.1364/MICROSCOPY.2022.MW3A.1.

[44] O. A. Zyuryukina and D. A. ShvaZyuryukina, O. A., Shvachkina, M. E., Kochubey, V. I., Sinichkin, Y. P., & Yakovlev, "Testing the adequacy of a simple theoretical model of dehydration optical clearing of collagen bundles: OCT measurements," *Quantum Electron.*, vol. 52, no. 1, p. 48, 2022, doi: 10.1070/QEL17965.

[45] M. Endrizzi, "X-ray phase-contrast imaging," *Nucl. Inst. Methods Phys. Res. A*, vol. 878, pp. 88–98, 2018, doi: 10.1016/j.nima.2017.07.036.

[46] H. Dejea *et al.*, "Synchrotron X-Ray Phase Contrast Imaging and Deep Neural Networks for Cardiac Collagen Quantification in Hypertensive Rat Model BT," in *International Conference on Functional Imaging and Modeling of the Heart*, 2019, pp. 187–195.

[47] A. Horng *et al.*, "Multiscale X-ray phase contrast imaging of human cartilage for investigating osteoarthritis formation," *J. Biomed. Sci.*, vol. 28, no. 1, pp. 1–14, 2021, doi: 10.1186/s12929-021-00739-1.

[48] A. Bravin, P. Coan, and P. Suortti, "X-ray phase-contrast imaging: From pre-clinical applications towards clinics," *Phys. Med. Biol.*, vol. 58, no. 1, 2013, doi: 10.1088/0031-9155/58/1/R1.

[49] T. Donath, F. Pfeiffer, C. Gru, E. Hempel, and C. David, "Toward Clinical X-ray Phase-Contrast CT," vol. 45, no. 7, 2010.

[50] M. Furlani, N. Riberti, M. L. Gatto, and A. Giuliani, "High-Resolution Phase-Contrast Tomography on Human Collagenous Tissues: A Comprehensive Review," *Tomography*, vol. 9, no. 6, pp. 2116–2133, 2023, doi: 10.3390/tomography9060166.

[51] L. Quenot, S. Bohic, and E. Brun, "X-ray Phase Contrast Imaging from Synchrotron to Conventional Sources: A Review of the Existing Techniques for Biological Applications," *Appl. Sci.*, vol. 12, no. 19, 2022, doi: 10.3390/app12199539.

[52] D. Paganin, S. C. Mayo, T. E. Gureyev, P. R. Miller, and S. W. Wilkins, "Simultaneous phase and amplitude extraction from a single defocused image of a homogeneous object," *J. Microsc.*, vol. 206, no. 1, pp. 33–40, 2002, doi: 10.1046/j.1365-2818.2002.01010.x.

[53] C. Zuo *et al.*, "Transport of intensity equation: a tutorial," *Opt. Lasers Eng.*, vol. 135, no. May, 2020, doi: 10.1016/j.optlaseng.2020.106187.

[54] X. Wu, H. Liu, and A. Yan, "X-ray phase-attenuation duality and phase retrieval," *Opt. Lett.*, vol. 30, no. 4, pp. 379–381, 2005.

[55] P. Villanueva-Perez, F. Arcadu, P. Cloetens, and M. Stampanoni, "Contrast-transfer-function phase retrieval based on compressed sensing," *Opt. Lett.*, vol. 42, no. 6, pp. 1133–1136, 2017.

[56] C. Metzler, P. Schniter, A. Veeraraghavan, and R. Baraniuk, "prDeep: Robust phase retrieval with a flexible deep network," in *International Conference on Machine Learning*, 2018, pp. 3501–3510.

[57] Y. Wu, Y. Guo, H. Bao, and C. Rao, "Sub-millisecond phase retrieval for phase-diversity wavefront sensor," *Sensors*, vol. 20, no. 17, p. 4877, 2020.

[58] D. Orsuti *et al.*, "Deep learning-based phase retrieval scheme for minimum-phase signal recovery," *J. Light. Technol.*, vol. 41, no. 2, pp. 578–592, 2023.

[59] H. Yan, "Ptychographic phase retrieval by proximal algorithms," *New J. Phys.*, vol. 22, no. 2, p. 23035, 2020.

[60] K. Mom, M. Langer, and B. Sixou, "Nonlinear primal--dual algorithm for the phase and absorption retrieval from a single phase contrast image," *Opt. Lett.*, vol. 47, no. 20, pp. 5389–5392, 2022, doi: 10.1364/OL.469174.

[61] K. A. Mohan, S. Member, J. Forien, V. Sridhar, J. Cuadra, and D. Parkinson, "Maximum Likelihood based Phase-Retrieval using Fresnel Propagation Forward Models with Optional Constraints," *IEEE Trans. Comput. IMAGING*, vol. 9, pp. 1–19, 2023, doi:

10.1109/TCI.2023.3332007.

[62] R. Schofield *et al.*, "Image reconstruction: Part 1–understanding filtered back projection, noise and image acquisition," *J. Cardiovasc. Comput. Tomogr.*, vol. 14, no. 3, pp. 219–225, 2020.

[63] L. Liu, "Model-based iterative reconstruction: a promising algorithm for today's computed tomography imaging," *J. Med. imaging Radiat. Sci.*, vol. 45, no. 2, pp. 131–136, 2014.

[64] J. Feng, Q. Sun, Z. Li, Z. Sun, and K. Jia, "Back-propagation neural network-based reconstruction algorithm for diffuse optical tomography," *J. Biomed. Opt.*, vol. 24, no. 5, p. 51407, 2019.

[65] D. Wu, K. Kim, and Q. Li, "Computationally efficient deep neural network for computed tomography image reconstruction," *Med. Phys.*, vol. 46, no. 11, pp. 4763–4776, 2019, doi: 10.1002/mp.13627.

[66] H. Lee, J. Lee, H. Kim, and B. Cho, "Deep-Neural-Network-Based Sinogram Synthesis for Sparse-View CT Image Reconstruction," *IEEE Trans. Radiat. Plasma Med. Sci.*, vol. 3, no. 2, pp. 109–119, 2019, doi: 10.1109/TRPMS.2018.2867611.

[67] P. V. P. M. Langer, K. Mom, M. Furlani, A. Giuliani, B. Sixou, "PyPhase – current developments of the phase retrieval Python package," *Abstr. Face2Phase*.

[68] C. P. Denton and D. Khanna, "Systemic sclerosis," *Lancet*, vol. 390, no. 10103, pp. 1685–1699, 2017, doi: 10.1016/S0140-6736(17)30933-9.

[69] S. I. Nihtyanova and C. P. Denton, "Pathogenesis of systemic sclerosis associated interstitial lung disease," *J. Scleroderma Relat. Disord.*, vol. 5, no. 2, pp. 6–16, 2020, doi: 10.1177/2397198320903867.

[70] N. C. Henderson, F. Rieder, and T. A. Wynn, "Fibrosis: from mechanisms to medicines," *Nature*, vol. 587, no. 7835, pp. 555–566, 2020, doi: 10.1038/s41586-020-2938-9.

[71] C. Paolini, S. Agarbati, D. Benfaremo, M. Mozzicafreddo, S. Svegliati, and G. Moroncini, "PDGF/PDGFR: A Possible Molecular Target in Scleroderma Fibrosis," *Int. J. Mol. Sci.*, vol. 23, no. 7, 2022, doi: 10.3390/ijms23073904.

[72] S. Svegliati Baroni *et al.*, "Stimulatory Autoantibodies to the PDGF Receptor in Systemic Sclerosis," *N. Engl. J. Med.*, pp. 2667–2676, 2006.

[73] F. Brun *et al.*, "SYRMEP Tomo Project: a graphical user interface for customizing CT reconstruction workflows," *Adv. Struct. Chem. Imaging*, vol. 3, no. 1, 2017, doi: 10.1186/s40679-016-0036-8.

[74] J. Schindelin *et al.*, "Fiji: an open-source platform for biological-image analysis," *Nat. Methods*, vol. 9, no. 7, pp. 676–682, 2012, doi: 10.1038/nmeth.2019.

[75] N. L. Fazzalari and I. H. Parkinson, "Fractal dimension and architecture of trabecular bone," *J. Pathol.*, vol. 178, no. 1, pp. 100–105, 1996, doi: 10.1002/(SICI)1096-

9896(199601)178:1<100::AID-PATH429>3.0.CO;2-K.

[76] O. I. Protic Md Soriful; Greco, Stefania; Giannubilo, Stefano Raffaele; Lamanna, Pasquale; Petraglia, Felice; Ciavattini, Andrea; Castellucci, Mario; Hinz, Boris; Ciarmela, Pasquapina, "Activin A in Inflammation, Tissue Repair, and Fibrosis: Possible Role as Inflammatory and Fibrotic Mediator of Uterine Fibroid Development and Growth," *Semin Reprod Med*, vol. 35, no. 06, pp. 499–509, 2017, doi: 10.1055/s-0037-1607265.

[77] A. Giuliani *et al.*, "Advanced 3D Imaging of Uterine Leiomyoma's Morphology by Propagation-based Phase-Contrast Microtomography," *Sci. Rep.*, vol. 9, no. 1, pp. 1–11, 2019, doi: 10.1038/s41598-019-47048-0.

[78] S. W. Weiss, "Smooth Muscle Tumors of Soft Tissue," *Adv. Anat. Pathol.*, vol. 9, no. 6, 2002, [Online]. Available: https://journals.lww.com/anatomicpathology/fulltext/2002/11000/smooth_muscle_tumors_of_soft_tissue.4.aspx.

[79] A. Belloni *et al.*, "Uterine leiomyoma as useful model to unveil morphometric and macromolecular collagen state and impairment in fibrotic diseases: An ex-vivo human study," *Biochim. Biophys. Acta - Mol. Basis Dis.*, vol. 1868, no. 12, p. 166494, 2022, doi: 10.1016/j.bbadis.2022.166494.

[80] G. E. Romanos, C. Schröter-Kermani, D. Weingart, and J. R. Strub, "Healthy Human Periodontal Versus Peri-implant Gingival Tissues: An Immunohistochemical Differentiation of the Extracellular Matrix.," *Int. J. Oral Maxillofac. Implants*, vol. 10, no. 6, 1995.

[81] A. Sculean, R. Gruber, and D. D. Bosshardt, "Soft tissue wound healing around teeth and dental implants," *J. Clin. Periodontol.*, vol. 41, pp. S6–S22, 2014, doi: 10.1111/jcpe.12206.

[82] M. Nevins, M. Camelo, M. L. Nevins, P. Schupbach, and D. M. Kim, "Connective tissue attachment to laser-microgrooved abutments: a human histologic case report.," *Int. J. Periodontics Restorative Dent.*, vol. 32, no. 4, 2012.

[83] T. Berglundh, S. Jepsen, B. Stadlinger, and H. Terheyden, "Peri-implantitis and its prevention," *Clin. Oral Implants Res.*, vol. 30, no. 2, pp. 150–155, 2019, doi: 10.1111/clr.13401.

[84] L. Canullo, A. Giuliani, M. Furlani, M. Menini, A. Piattelli, and G. Iezzi, "Influence of abutment macro- and micro-geometry on morphologic and morphometric features of peri-implant connective tissue," *Clin. Oral Implants Res.*, no. May, pp. 1–14, 2023, doi: 10.1111/clr.14118.

[85] G. Iezzi, F. Di Lillo, M. Furlani, M. Degidi, A. Piattelli, and A. Giuliani, "The symmetric 3d organization of connective tissue around implant abutment: A key-issue to prevent bone resorption," *Symmetry (Basel).*, vol. 13, no. 7, pp. 1–12, 2021, doi: 10.3390/sym13071126.

[86] L. Togni *et al.*, "The Emerging Impact of Tumor Budding in Oral Squamous Cell Carcinoma: Main Issues and Clinical Relevance of a New Prognostic Marker," *Cancers*

(Basel)., vol. 14, no. 15, 2022, doi: 10.3390/cancers14153571.

[87] M. Mascitti *et al.*, "Addition of the tumour–stroma ratio to the 8th edition American Joint Committee on Cancer staging system improves survival prediction for patients with oral tongue squamous cell carcinoma," *Histopathology*, vol. 77, no. 5, pp. 810–822, 2020, doi: 10.1111/his.14202.

[88] R. M. Bremnes *et al.*, "The role of tumor stroma in cancer progression and prognosis: Emphasis on carcinoma-associated fibroblasts and non-small cell lung cancer," *J. Thorac. Oncol.*, vol. 6, no. 1, pp. 209–217, 2011, doi: 10.1097/JTO.0b013e3181f8a1bd.

[89] A. Almangush *et al.*, "Clinical significance of tumor-stroma ratio in head and neck cancer: a systematic review and meta-analysis," *BMC Cancer*, vol. 21, no. 1, pp. 1–8, 2021, doi: 10.1186/s12885-021-08222-8.

[90] A. Devendra, K. C. Niranjan, A. Swetha, and H. Kaveri, "Histochemical analysis of collagen reorganization at the invasive front of oral squamous cell carcinoma tumors," *J. Investig. Clin. Dent.*, vol. 9, no. 1, pp. 1–8, 2018, doi: 10.1111/jicd.12283.

[91] M. Yu *et al.*, "Upregulated LOX and increased collagen content associated with aggressive clinicopathological features and unfavorable outcome in oral squamous cell carcinoma," *J. Cell. Biochem.*, vol. 120, no. 9, pp. 14348–14359, 2019, doi: 10.1002/jcb.28669.

[92] S. Samyukta, A. H. R. H. Priya, S. M. Kumar, and V. L. P. Sri, "An Evaluation of the Prognosticative Value of Hyalinization in the Biological Behaviour of Oral Lesions Using Image Analysis," *Asian Pacific J. Cancer Prev.*, vol. 23, no. 8, pp. 2829–2834, 2022, doi: 10.31557/APJCP.2022.23.8.2829.

[93] R. Sharma *et al.*, "Architectural analysis of picrosirius red stained collagen in oral epithelial dysplasia and oral squamous cell carcinoma using polarization microscopy," *J. Clin. Diagnostic Res.*, vol. 9, no. 12, pp. EC13–EC16, 2015, doi: 10.7860/JCDR/2015/13476.6872.

[94] F. H. Silver, "Mechanotransduction-The relationship between gravity, cells and tensile loading in extracellular matrix," *Biocell*, vol. 46, no. 2, pp. 297–299, 2022, doi: 10.32604/biocell.2022.017406.

[95] R. Chetambath and N. Ravindran, "Mechanotransduction in fibrosis," *J. Adv. Lung Heal.*, vol. 3, no. 2, p. 79, 2023, doi: 10.4103/jalh.jalh_1_23.

[96] E. Brauer *et al.*, "Collagen Fibrils Mechanically Contribute to Tissue Contraction in an In Vitro Wound Healing Scenario," *Adv. Sci.*, vol. 6, no. 9, 2019, doi: 10.1002/advs.201801780.

[97] N. Riberti *et al.*, "Deep Learning for Microstructural Characterization of Synchrotron Radiation-Based Collagen Bundle Imaging in Peri-Implant Soft Tissues," *Appl. Sci.*, 2023.

[98] D. Li *et al.*, "The added effect of artificial intelligence on physicians' performance in detecting thoracic pathologies on CT and chest X-ray: A systematic review," *Diagnostics*, vol. 11, no. 12, 2021, doi: 10.3390/diagnostics11122206.

[99] A. Sharma, S. Rani, and D. Gupta, "Artificial Intelligence-Based Classification of Chest X-Ray Images into COVID-19 and Other Infectious Diseases," *Int. J. Biomed. Imaging*, vol. 2020, 2020, doi: 10.1155/2020/8889023.

[100] B. Hunter, S. Hindocha, and R. W. Lee, "The Role of Artificial Intelligence in Early Cancer Diagnosis," *Cancers (Basel).*, vol. 423 LNNS, pp. 530–542, 2022, doi: https://doi.org/10.3390/cancers14061524.

[101] F. Pfeiffer, T. Weitkamp, O. Bunk, and C. David, "Phase retrieval and differential phase-contrast imaging with low-brilliance X-ray sources," *Nat. Phys.*, vol. 2, no. 4, pp. 258–261, 2006, doi: 10.1038/nphys265.

[102] T. Tuohimaa, M. Otendal, and H. M. Hertz, "Phase-contrast x-ray imaging with a liquid-metal-jet-anode microfocus source," *Appl. Phys. Lett.*, vol. 91, no. 7, p. 74104, Aug. 2007, doi: 10.1063/1.2769760.

[103] A. Tkachuk, F. Duewer, H. Cui, M. Feser, S. Wang, and W. Yun, "X-ray computed tomography in Zernike phase contrast mode at 8 keV with 50-nm resolution using Cu rotating anode X-ray source," *Zeitschrift fur Krist.*, vol. 222, no. 11, pp. 650–655, 2007, doi: 10.1524/zkri.2007.222.11.650.

[104] M. Eckermann, M. Töpperwien, A.-L. Robisch, F. van der Meer, C. Stadelmann, and T. Salditt, "Phase-contrast x-ray tomography of neuronal tissue at laboratory sources with submicron resolution," *J. Med. Imaging*, vol. 7, no. 01, p. 1, 2020, doi: 10.1117/1.jmi.7.1.013502.

[105] A. Momose, "X-ray phase imaging reaching clinical uses," *Phys. Medica*, vol. 79, no. October, pp. 93–102, 2020, doi: 10.1016/j.ejmp.2020.11.003.

Appendix 1

New functionality implemented in the *PyPhase dataset module* to directly read SYRMEP beamline (Elettra Synchrotron, Trieste) files, in order to be able to take advantage of all the algorithms available in the package, even without any knowledge of how the information is stored inside the file.

– – –

```
class Elettra(Dataset, backend):
    """Class for raw Elettra Synchrotron data sets.

    Attributes
    ----------
    ztot : float
        Focus to detector distance in m.
    path : str
        Path to dataset.
    version : str
        Version of Dataset backend structure, e.g. 'TIEHOM'
    name : str
        Name of dataset
    projection_prefix : str
        HDF5 path to projection data.
    reference_position : int
        Position number as reference for alignment (usually highest resolution)
    darkfield_prefix : str
        HDF5 path prefix to darkfields
    flatfield_prefix : str
        HDF5 path prefix to flatfields
    aligned : int
        Flag if dataset is aligned or not.
    """

    def __init__(self, name: str, path: str = '.', version: str = 'ḿaster'):

        self.path = path
        self.version = version
        self.name = name

        self.data_basename = self.path + '/' + self.name  # TODO: Attribute?
```

```
        self.dataset_filename = pyphase_path / (self.name + '_' + self.version + '.tdf')  # TODO: Attribute?

        self.projection_prefix = 'exchange/data'

        self.correct_alignment = 1

        self.ztot = 20  # Focus to detector distance in m
        #self.z2 = 'entry/instrument/detector/distance/' # Sample to detector distance in mm
        self.measurement_prefix = 'provenance/detector_output/'
        self.pixel_size_filename = path + '/' 'pixelsize.txt'
        self.darkfield_prefix = 'exchange/data_dark/'
        self.flatfield_prefix = 'exchange/data_white/'

        self.aligned = 0  # TODO: Should be bool

        super().__init__(name, path, version)
        self.reference_position = 0

    def read_parameters_frontend(self):
        if os.path.isfile(self.pixel_size_filename):
            print('Text file with scan parameters found!')
            # self.Initialise()
            # TODO: STub. Should take values from the data h5 file
            with open(self.pixel_size_filename) as pixel_size_file:
                lines = pixel_size_file.readlines()

            del lines[0]  # remove header line
            self.nD = len(lines)
            self.position_number = np.arange(1, self.nD + 1).tolist()
            self.pixel_size_x = np.zeros(len(lines))
            self.pixel_size_y = np.zeros_like(self.pixel_size_x)
            self.z2 = np.zeros_like(self.pixel_size_x)

            for n, line in enumerate(lines):
                line = line.split()
                self.pixel_size_x[n] = float(line[1])
                self.pixel_size_y[n] = float(line[2])
                self.z2[n] = float(line[0])
                self.energy = float(line[3])
                pass
        else:
            print('No text file with scan parameters found!\nEnter required parameters:\n')
            self.energy = float(input('Insert energy in KeV: '))
```

```
            self.pixel_size_x = float(input('Insert pixel size x in um: '))
            self.pixel_size_y = float(input('Insert pixel size y in um: '))
            self.z2 = float(input('Insert Sample-Detector distance in cm: '))


        self.z2 = self.z2 / 1e3 #z2 in m
        self.z1 = self.ztot- self.z2 # Fucus to sample distance in m
        self.effective_distance = self.z1 * self.z2 / (self.z1 + self.z2)

        # Read parameters from data file
        projection_data_filename = self.data_basename + '.tdf'
        with h5py.File(projection_data_filename, 'r') as data_file:
            self.number_of_projections = data_file[self.projection_prefix].shape[1]
            self.nx = data_file[self.projection_prefix].shape[2]
            self.ny = data_file[self.projection_prefix].shape[0]
            # Calculate dark and flat references
            dark_images = data_file[self.darkfield_prefix][:]
            flat_images = data_file[self.flatfield_prefix][:]

        dark_image = np.median(dark_images, axis=1)
        flat_image = np.median(flat_images, axis=1)
        backend.write_image(self, image=dark_image, projection=0, projection_type='darkfield')
        backend.write_image(self, image=flat_image, projection=0, projection_type='flatfield')

    def get_projection(self, *, projection, position=0, pad=True, magnification=True, aligned=True,
Fourier=False):
        """
        Read one recorded image.

        Parameters
        ----------
        projection : int
            Number of projection to read.
        position : int
            Number of positiion ("distance") to read.
        pad : bool, optional
            Pads the image.
        magnification : bool, optional
            Brings the image to the magnification of reference_position.
        aligned : bool, optional
            Corrects alignment (requires alignment of projections).
        Fourier : bool
            Returns the Fourier transform of the image.
```

```
    """
    while True:
        try:
            with h5py.File(self.data_basename + '.tdf', 'r') as f:
                projection_image = f[self.projection_prefix][:, projection, :]  # Read projection
                break  # Success!
        except OSError:
            time.sleep(1)  # Wait a bit

    flat_image = self.get_image(projection=0, image_type='flat')
    dark_image = self.get_image(projection=0, image_type='dark')
    projection_image = (projection_image-dark_image) / (flat_image-dark_image)

    # Zoom images to same scale, corresponding to highest magnification
    if position != self.reference_position and magnification:  # TODO: should implement distance_number, but YAGN?
        projection_image = ndimage.zoom(projection_image,
                                        [1 / self.magnification_y[position],
                                         1 / self.magnification_x[position]],
                                        mode='nearest')  # Zoom to highest magnification TODO: combine w/ alignment?

    # Correct alignment
    if aligned and self.aligned and position != self.reference_position:
        transform_parameters = self.get_alignment(projection=projection,
                                                  position=position)  # Get alignment parameters TODO: add zoom factor here?
        projection_image = registrator.apply_transformation(projection_image, transform_parameters)

    if Fourier:
        projection_image = Utilities.resize(projection_image, (self.nfy, self.nfx))
        return np.fft.fft2(projection_image)
    else:
        if pad:
            return Utilities.resize(projection_image, (self.nfy, self.nfx))
        else:
            return Utilities.resize(projection_image, (self.ny, self.nx))
```